NAVAL POSTGRADUATE SCHOOL

MONTEREY, CALIFORNIA

THESIS

PROTOTYPING AND CHARACTERIZATION OF AN ADJUSTABLE SKEW ANGLE SINGLE GIMBAL CONTROL MOMENT GYROSCOPE

by

Shawn M. Kocis

March 2015

Thesis Advisor:	Mark Karpenko
Second Reader:	I. Michael Ross

THIS PAGE INTENTIONALLY LEFT BLANK

REPORT DOCUMENTATION PAGE

Form Approved OMB No. 0704–0188

1. AGENCY USE ONLY *(Leave blank)*	2. REPORT DATE	3. REPORT TYPE AND DATES COVERED
	March 2015	Master's Thesis

4. TITLE AND SUBTITLE
PROTOTYPING AND CHARACTERIZATION OF AN ADJUSTABLE SKEW ANGLE SINGLE GIMBAL CONTROL MOMENT GYROSCOPE

5. FUNDING NUMBERS

. AUTHOR(S) Shawn M. Kocis

7. PERFORMING ORGANIZATION NAME(S) AND ADDRESS(ES)
Naval Postgraduate School
Monterey, CA 93943–5000

8. PERFORMING ORGANIZATION REPORT NUMBER

9. SPONSORING /MONITORING AGENCY NAME(S) AND ADDRESS(ES)
N/A

10. SPONSORING/MONITORING AGENCY REPORT NUMBER

11. SUPPLEMENTARY NOTES The views expressed in this thesis are those of the author and do not reflect the official policy or position of the Department of Defense or the U.S. Government. IRB Protocol number ____N/A____.

12a. DISTRIBUTION / AVAILABILITY STATEMENT
Approved for public release; distribution is unlimited

12b. DISTRIBUTION CODE

13. ABSTRACT (maximum 200 words)

This thesis is the second phase of development of an open architecture control moment gyroscope (CMG). The focus is on designing an adjustable skew angle single gimbal CMG frame, and integrating a previously developed momentum wheel assembly into it. The result of this phase is a fully operational CMG that can be used to retrofit the NPS Reconfigurable Satellite Autonomy Testbed (R-SAT). The open architecture design allows for both hardware and software upgrades to the R-SAT Attitude Determination and Control System (ADCS). This capability is vitally important in order to support the development and testing of new satellite control algorithms that can be used to improve the agility and efficiency of satellite maneuvers. The CMG developed in this project is capable of delivering 7.79 Nm of output torque at the standard gimbal rate of 1 rad/s. The CMG power consumption ranges between 50W and 100W.

4. SUBJECT TERMS Control Moment Gyroscope, Control Moment Gyro, gimbal, momentum wheel, momentum wheel assembly, skew angle, adjustable skew angle, back drive, open architecture

15. NUMBER OF PAGES
103

16. PRICE CODE

17. SECURITY CLASSIFICATION OF REPORT	18. SECURITY CLASSIFICATION OF THIS PAGE	19. SECURITY CLASSIFICATION OF ABSTRACT	20. LIMITATION OF ABSTRACT
Unclassified	Unclassified	Unclassified	UU

NSN 7540–01–280–5500

Standard Form 298 (Rev. 2–89)
Prescribed by ANSI Std. 239–18

THIS PAGE INTENTIONALLY LEFT BLANK

Approved for public release; distribution is unlimited

PROTOTYPING AND CHARACTERIZATION OF AN ADJUSTABLE SKEW ANGLE SINGLE GIMBAL CONTROL MOMENT GYROSCOPE

Shawn M. Kocis, Lieutenant Commander, United States Navy
B.S., Drexel University, 2003

Submitted in partial fulfillment of the
requirements for the degree of

MASTER OF SCIENCE IN ASTRONAUTICAL ENGINEERING

from the

NAVAL POSTGRADUATE SCHOOL
March 2015

Author: Shawn M. Kocis

Approved by: Mark Karpenko
Thesis Advisor

I. Michael Ross
Second Reader

Garth V. Hobson
Chair, Department of Mechanical and Aerospace Engineering

THIS PAGE INTENTIONALLY LEFT BLANK

ABSTRACT

This thesis is the second phase of development of an open architecture control moment gyroscope (CMG). The focus is on designing an adjustable skew angle single gimbal CMG frame, and integrating a previously developed momentum wheel assembly into it. The result of this phase is a fully operational CMG that can be used to retrofit the NPS Reconfigurable Satellite Autonomy Testbed (R-SAT). The open architecture design allows for both hardware and software upgrades to the R-SAT Attitude Determination and Control System (ADCS). This capability is vitally important in order to support the development and testing of new satellite control algorithms that can be used to improve the agility and efficiency of satellite maneuvers. The CMG developed in this project is capable of delivering 7.79 Nm of output torque at the standard gimbal rate of 1 rad/s. The CMG power consumption ranges between 50W and 100W.

THIS PAGE INTENTIONALLY LEFT BLANK

TABLE OF CONTENTS

LIST OF FIGURES

LIST OF TABLES

THIS PAGE INTENTIONALLY LEFT BLANK

LIST OF ACRONYMS AND ABBREVIATIONS

ADCS	attitude determination and control system
BASS	break-away support system
BBB	BeagleBone Black
CAD	computer aided design
CAN	controller area network
CCW	counter clockwise
CW	clockwise
CMG	control moment gyroscope
DC	direct current
DOF	degrees of freedom
FDM	fused deposition modeling
GUI	graphical user interface
IMU	inertial measurement unit
I/O	input/output
MOI	moment of inertia
NiCd	nickel cadmium
NPS	Naval Postgraduate School
rpm	revolutions per minute
R-SAT	reconfigurable satellite testbed
SBC	single board computer
USB	universal serial bus
VDC	volts direct current
VSCMG	variable speed control moment gyroscope

THIS PAGE INTENTIONALLY LEFT BLANK

ACKNOWLEDGMENTS

I would like to begin by thanking the Naval Postgraduate School and the Space Systems Academic Group for the incredible faculty support and high-quality facilities. Specifically, I would like to thank Dr. Mark Karpenko for the many hours that he spent discussing this project with me, and pointing me in the right direction at the times when I reached the extent of my knowledge of some of the unexpected intricacies of a CMG. His work in advising me on this project has helped me to greatly broaden my knowledge base.

To say that the results of this project would not have been possible without the help of Mr. Jim Horning would be a serious understatement. Jim was truly instrumental during the months of wireless communication system troubleshooting that I had to do during this project. Once the decision was made to incorporate a flight computer vice direct wireless communications, it was his software coding of the BeagleBone Black flight computer that made the CMG testbed come alive. If it were not for his help, I would still be trying to learn how to program in Python rather than having a fully functioning CMG on which to conduct tests.

Last, but certainly not least, I would like to thank my family. The love and support of my parents, my wife Nathalie, and my sons Alex and Zac, have given me strength in the toughest of times. To my boys, I hope that the excitement that we shared as we watched this project progress will inspire you to always keep learning, and never give up on your dreams.

THIS PAGE INTENTIONALLY LEFT BLANK

I. INTRODUCTION

A. BACKGROUND AND MOTIVATION

The advancements in modern computer processing have provided the opportunity to develop and use control systems which were previously considered to be too costly or even impossible to implement for satellite maneuvering. Work conducted by groups, including those in the Naval Postgraduate School's (NPS) Control and Optimization Laboratories, have shown that optimal control trajectories can be planned and executed by current on-orbit systems. These systems, however, use control algorithms and constraints developed decades earlier based on linearized control models aimed at simplifying and reducing computing requirements. On-orbit demonstrations have been conducted on spacecraft such as the International Space System [1], and NASA's TRACE [2] to show that these optimal trajectories can be planned and executed even using legacy Attitude Determination and Control Systems (ADCS). Unfortunately, these legacy systems cannot take full advantage of the benefits of optimal control because the underlying control systems are inherently designed to perform standard maneuvers, as shown in Figure 1.

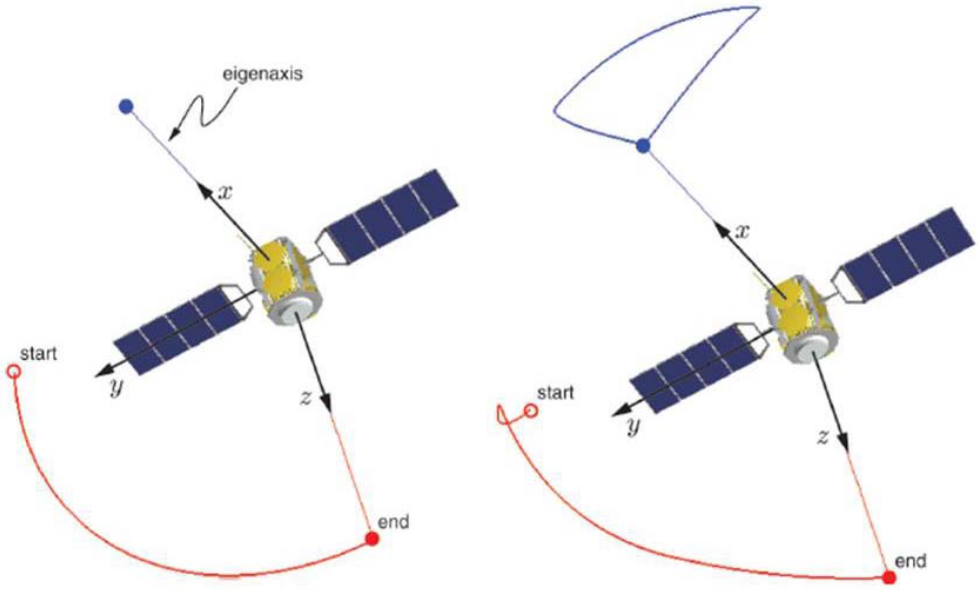

Figure 1. TRACE maneuvers, (left) standard, (right) new time-optimal, after [2]

In order to demonstrate, on physical hardware, the ability to implement these new control algorithms and techniques for improved system maneuvering a reconfigurable, open architecture control system is necessary to illustrate the full advantage of these advanced control concepts. This thesis project is the second phase in a project to develop an open architecture control moment gyroscope (CMG) that will be installed in a CMG array on a satellite simulator testbed to support development and testing of a next generation ADCS that can fully integrate newly developed control algorithms as part of the flight software.

B. THESIS OBJECTIVES AND SCOPE

The first phase of this project was conducted by Kerri Ackman in 2012 [3]. Ackman's work focused on the design of a new open-architecture momentum wheel as the central component of a CMG based ADCS. This project addresses the second phase of this ADCS development by focusing on the design of the gimbal mechanism, and the integration of a complete prototype CMG. The project was conducted in three parts: (i) the design of the CMG gimbal assembly, (ii) the design of a single degree of freedom (DOF) testbed for system characterization testing, and (iii) the development and performance of the testing.

The primary objective of the project was to design and build an adjustable skew angle CMG gimbal frame that could incorporate the Ackman momentum wheel. The secondary objective was to run a series of characterization tests on the fully integrated CMG in order to determine the feasibility of its use in a satellite simulator. The scope of the primary objective lies in designing, building and integrating the CMG hardware. The second objective was initially constrained to testing of the CMG hardware, but the scope expanded throughout the project to include the design of the testbed infrastructure needed to perform the characterization tests.

C. THESIS OUTLINE

The remainder of the thesis is organized as follows. Chapter II focuses on the structural design of the CMG, and the mechanical drive train of the gimbal. Chapter III focuses on the electrical and electronic system design of the CMG. Chapter IV gives a

description of how the design process of the CMG leveraged 3D printing technology for rapid prototyping of parts for fit check and initial functional testing as well as for manufacturing a series of custom end item parts used in building the CMG testbed. Chapter V describes each of the tests that were performed in order to characterize the CMG performance, and an analysis of the test results is provided. In addition to the standard battery of CMG performance tests that were planned, a characterization of the CMG back drive phenomenon discussed in [4] was conducted. Chapter VI summarizes the work which was completed in the project, and discusses the next steps needed to integrate the CMG into the open-architecture ADCS.

THIS PAGE INTENTIONALLY LEFT BLANK

II. STRUCTURAL DESIGN

A. INTRODUCTION

In order to conduct testing of future control algorithms a next generation, open-architecture Reconfigurable Satellite Autonomy Testbed (R-SAT) is being developed. This new testbed will be largely based on the current NPS R-SAT, but will include a flexible open architecture ADCS. Due to the fact that this new system will be an evolution of the current testbed the components designed in this project needed to be physically compatible with the R-SAT deck. This chapter describes the design of the structural and mechanical components of the CMG.

B. DESIGN OBJECTIVES

The mounting locations and available space on the R-SAT, as well as the physical shape of the previously developed Ackman momentum wheel [3] provided constraints for the design of the CMG system. In conjunction with these constraints a set of design objectives were identified to guide the direction of the project. The three primary design objectives were to develop a CMG which can be upgraded as necessary with new components and software, is compatible with the Ackman wheel and R-SAT deck, and features a manually adjustable skew angle which will enable greater flexibility for experiments.

1. Reconfigurable Satellite Autonomy Testbed

The current NPS R-SAT, shown in Figure 2, is a 3-DOF satellite simulator testbed which was procured from Andrews Space Company in 2009 to allow for the testing of new satellite attitude control algorithms. The R-SAT uses four Variable Speed CMGs (VSCMG), shown in Figure 3, each with a fixed skew angle of 53.4°, a nominal angular momentum of 9.08 Nms, and a nominal maximum torque of 0.16 Nm/°/s [5] for its primary attitude control. Compressed gas thrusters are also available for secondary control and momentum management.

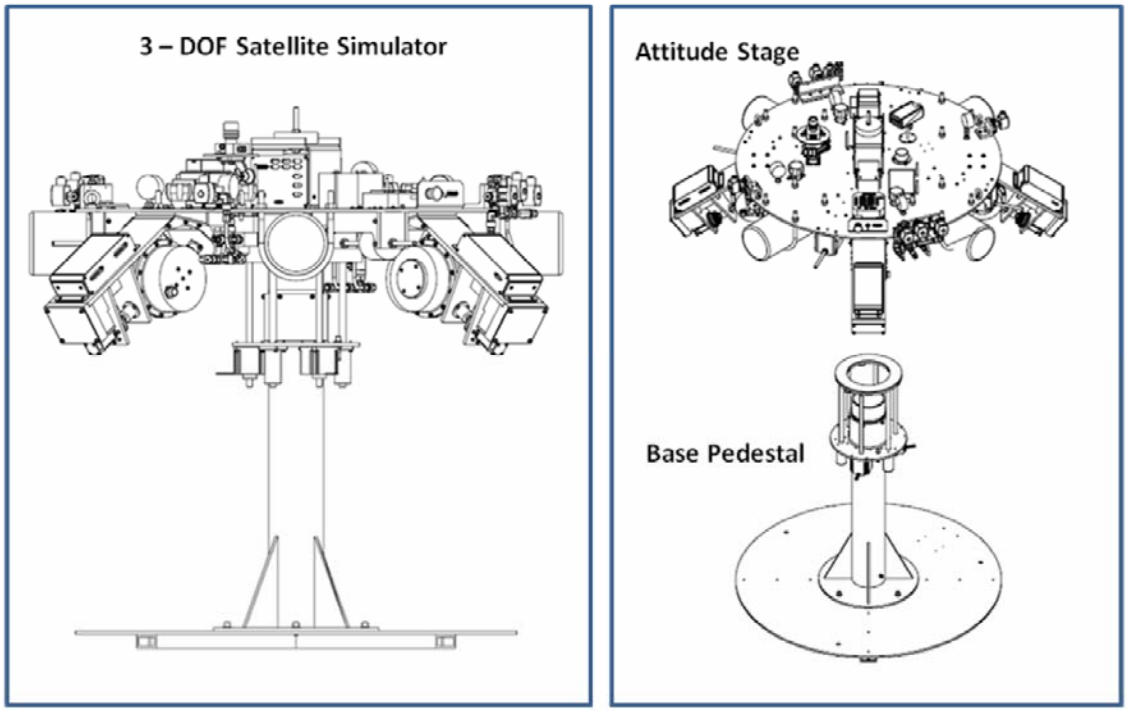

Figure 2. NPS Reconfigurable Satellite Testbed (R-SAT), from [5]

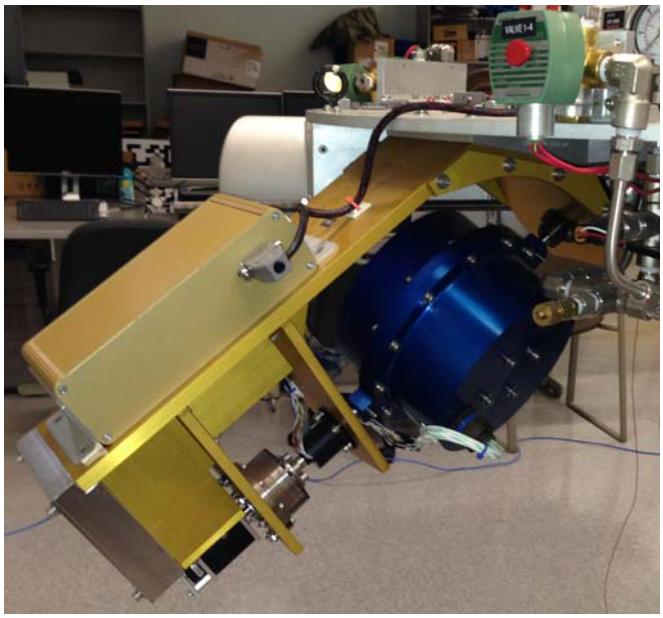

Figure 3. Andrews Space VSCMG

The characteristics of the individual CMGs are listed in Table 1, and were derived from the information given in [5]. Using the measured moment of inertia (I) for each wheel the angular momentum (h_0) for each of the four VSCMGs was calculated using Equation (1) with a nominal spin rate, ω = 680.678 rad/s (6500 rpm).

$$h_0 = I * \omega \tag{1}$$

CMG output torque (T) is calculated using Equation (2), where H is the angular momentum of the CMG, and $\dot{\delta}$ is the gimbal rate of the CMG, both taken in the spacecraft body fixed frame [6]. Vector H is defined by Equation (3), where β is the CMG skew angle and δ is the instantaneous gimbal angle of the momentum wheel. The gimbal rate vector in the body fixed frame is defined by Equation (4), taken from [7], where $\dot{\delta}_0$ is the gimbal rate about the gimbal axis.

$$T = H \times \dot{\delta} \tag{2}$$

$$H = h_0 \begin{bmatrix} -\cos\beta \sin\delta \\ \cos\delta \\ \sin\delta \sin\beta \end{bmatrix} \tag{3}$$

$$\dot{\delta} = \begin{bmatrix} \dot{\delta}_0 \sin\beta \\ 0 \\ \dot{\delta}_0 \cos\beta \end{bmatrix} \tag{4}$$

For evaluating the torque output of a single CMG, these equations were simplified by taking β = 90°, and δ = 0° (instantaneously). The resulting simplified equations are shown in Equations (5), (6), and (7).

$$H = \begin{bmatrix} 0 \\ h_0 \\ 0 \end{bmatrix} \tag{5}$$

$$\dot{\delta} = \begin{bmatrix} \dot{\delta}_0 \\ 0 \\ 0 \end{bmatrix} \tag{6}$$

$$T = -h_0 \dot{\delta} \hat{z} \tag{7}$$

Table 1. Andrews Space VSCMG parameters at 6500 rpm, after [5]

	Symbol	CMG 1	CMG 2	CMG 3	CMG 4
Moment of Inertia (kg-m^2)	I	0.01331	0.01320	0.01336	0.01349
Angular Momentum (Nms)	h_0	9.06	8.99	9.10	9.18
CMG Output Torque (Nm/°/s)	T	0.158	0.157	0.159	0.160

As one of the design objectives for this new CMG is to provide comparable performance to the Andrews CMGs, the values in Table 1 will be used for output torque comparison.

2. Fixed Skew Angle

One of the major shortcomings of the R-SAT, from a reconfigurability perspective, was that the CMG skew angles were essentially fixed at 53.4°. This specific skew angle value is not the problem, as this is one commonly used CMG skew angle for satellite systems. The real issue is in regard to the fact that it is a fixed value, and the R-SAT is a testbed whose purpose is to investigate new control algorithms with the most system flexibility possible. The solution for adjusting the skew angle provided by Andrews Space was a set of fixed shim plates, which provided a few alternate values for skew angles that could be used. These shims were wholly inadequate for the purpose of system flexibility, and provided only a very small subset of alternative skew angles, all of which were within a few degrees of 53.4°. Also, due to these plates being positioned between the VSCMG frame and the R-SAT deck, it is necessary to completely remove

the VSCMG assembly from the deck in order to swap adapter plates. This is a highly intrusive and impractical means for skew angle adjustment.

In order to implement CMG arrays like a box-array which uses a 90° skew angle, as well as other configurations, a variable skew angle system which could be easily adjusted was strongly preferred. While a simple process for skew angle adjustment was desired, the complexity necessary to implement a dual gimbal CMG system where one gimbal is used to set the skew angle and the other to gimbal the momentum wheel was considered too complex, and hence undesirable. A means to manually adjust the angle was therefore determined as the requirement.

C. MECHANICAL SYSTEM DESIGN

In general, every CMG consists of two primary subsystems, a momentum wheel and a gimbal mechanism with a series of components that make those subsystems perform the desired effect of transferring momentum to the spacecraft. The first step in the CMG design process was to evaluate the Ackman momentum wheel and the Andrews Space gimbal frame designs in order to identify specific system design constraints as well as aspects of the current design and/or components which could be reused.

1. Momentum Wheel

The Ackman wheel was designed and built in 2012 as an open architecture system which could be a drop-in replacement for the momentum wheel in the Andrews Space VSCMG. The subsystem is composed of the components shown in Figure 4 and consists primarily of a rotating brass momentum wheel and a commercially available electric motor.

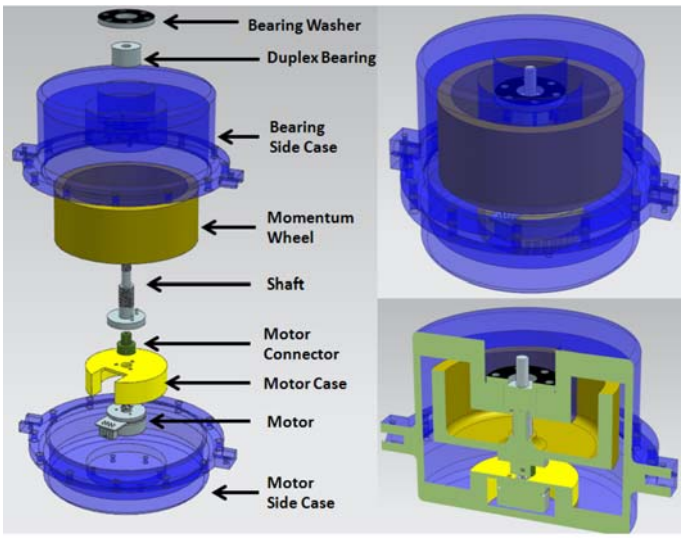

Figure 4. Momentum wheel assembly, from [3]

In order to compare the performance of the Ackman wheel to the Andrews wheel it was necessary to first compute the angular momentum and torque of the Andrews wheel at 5000 rpm, which is the maximum nominal speed of the Ackman wheel. The torque was calculated by entering the new spin rate ω = 523.598 rad/s (5000 rpm) into Equation (1) to determine h_0. The value of T for each wheel was then calculated with Equation (7). The results are listed in Table 2.

Table 2. Andrews Space VSCMG parameters at 5000 rpm, after [5]

	Symbol	CMG 1	CMG 2	CMG 3	CMG 4
Moment of Inertia (kg m^2)	I	0.01331	0.01320	0.01336	0.01349
Angular Momentum (Nms)	h_0	6.97	6.91	7.00	7.06
CMG Output Torque (Nm/°/s)	T	0.122	0.121	0.122	0.123

Once the reduced torques for the Andrews CMGs were calculated the same method was used to calculate T for the Ackman wheel. For this calculation the angular momentum values were calculated from the wheel MOI taken from [3]. The resulting values are listed in Table 3. These results indicate that although the Ackman wheel has a

lower maximum speed the performance is comparable to, and slightly exceeds, that of the Andrews wheels when each wheel is operated at the same nominal speed.

Table 3. Ackman wheel parameters at 5000 rpm

	Symbol	CMG 1
Moment of Inertia (kg m^2)	I	0.01483
Angular Momentum (Nms)	h_0	7.766
CMG Torque (Nm/°/s)	T	0.136

2. Gimbal Frame

The next step was to design the frame structure which houses the wheel and allows it to gimbal in order to transfer the wheel's momentum to the spacecraft simulator. The design process began with an inspection of the current Andrews Space CMG frame. Although the frame sufficiently met the basic system specifications, the desire to have an adjustable skew angle was a major driver in the redesign effort. The Andrews frame was built from anodized aluminum plates which measure 15.24 cm (6 in) across. The two vertical plates, which support the 100:1 ratio harmonic drive and the slip ring, on the right side of Figure 5 are 0.9525 cm (0.375 in) thick. The long horizontal plate at the top of Figure 5 and the vertical plate, which supports the needle bearing and optical encoder, on the left side of the image are 1.27 cm (0.5 in) thick. The 45° plate on the left side of the image, which connects the left vertical and top horizontal plates is 1.715 cm (0.675 in) thick. Attached to this plate is the silver colored aluminum adapter block which attaches between the R-SAT deck and the VSCMG. The spacer block provides the 53.4° VSCMG skew angle. In order to adjust the skew angle the entire CMG frame must be removed from the R-SAT deck, the skew angle spacer block must be replaced with a different spacer, and then the whole assembly reinstalled on the R-SAT.

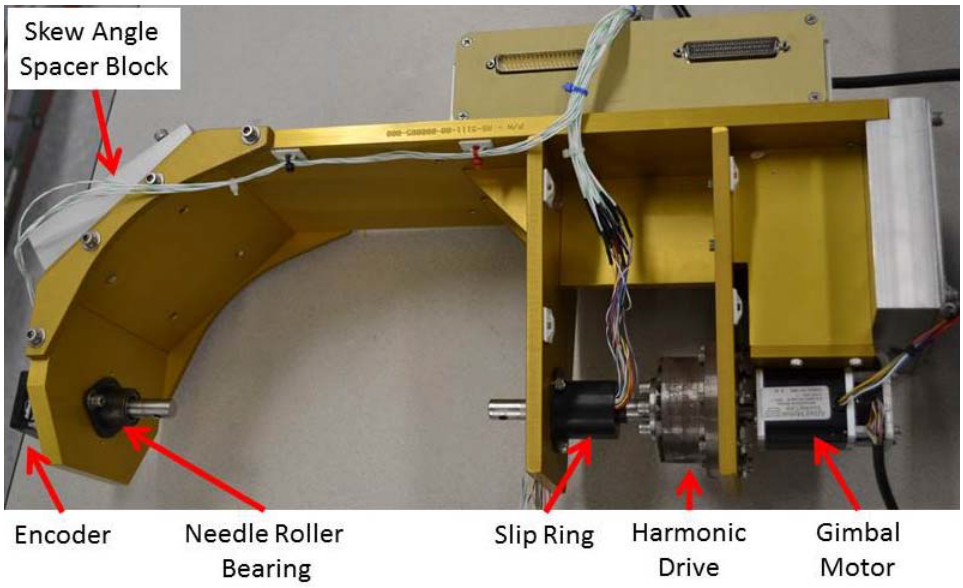

Figure 5. Andrews Space CMG frame

Following inspection of the Andrews frame, a number of design concepts were developed leveraging some of the existing components with a specific focus on a manually adjustable skew angle that does not require complete removal of the CMG from the R-SAT. The designs were mocked up using the Siemens NX 8.5 CAD software suite, and one of the early concepts is shown in Figure 6. This design used a series of 45° angled plates which could be easily bolted together into a 360° octagonal enclosure type of housing. The intent for this design was to enable the use of the frame to set the skew angle, as the system could be rotated around the full 360° frame. Although the initial concept had merit, and was similar to the circular cage type housings used on many satellite CMGs, the design had some shortcomings for this specific implementation. The two primary issues were 1) in order to facilitate unrestricted rotation some sort of slip ring would be necessary to connect the CMG motor wires to the momentum wheel motor, and 2) the Gimbal motor and encoder would have to be attached external to the frame and would cause the mounting frame to have to extend even further below the R-SAT deck to support the full range of motion.

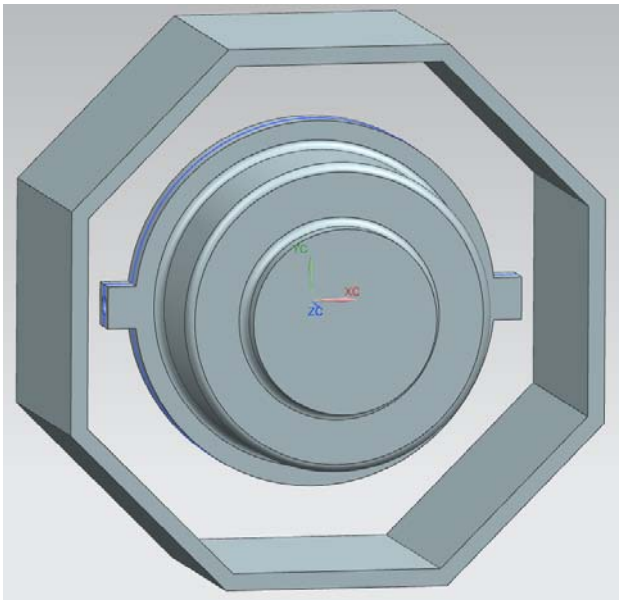

Figure 6. Early gimbal frame concept

While considering this design, it was identified that a full 360° rotation does not provide a level of benefit that is commensurate with the additional complexity necessary to implement it. The primary driver in this decision is the fact that the skew angle is the same whether it points the gimbal axis toward the +z or the –z axes of the R-SAT. What this essentially means is that the full 360° rotation was unnecessary, and that the ability to rotate the assembly through angles even less than 180° provides access to any skew angle that is desired. Following these observations, a modification was made to remove the lower three plates, creating a U-shaped gimbal frame, as shown in Figure 7.

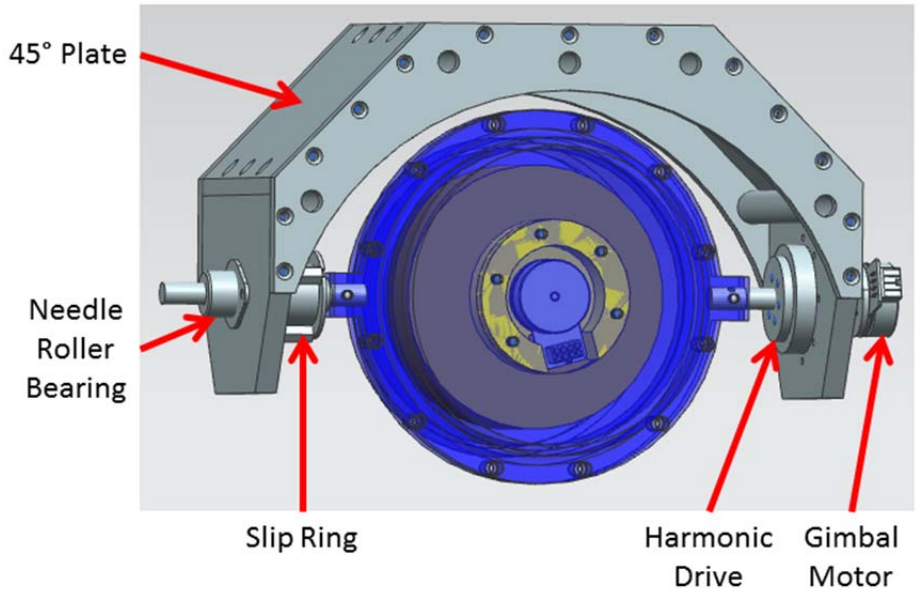

Figure 7. First gimbal frame prototype

The new design concept incorporated the 45° angled sides, a pair of curved support plates to provide structural rigidity and hold the frame plates in their correct locations, a brushless motor similar to the one used in the momentum wheel, as well as the gimbal shaft needle bearing, slip ring and 100:1 harmonic drive salvaged from the original Andrews design. An integral part of the adjustable skew angle mechanism for this design was a series of five hollow tubes that provided both additional stiffness to the frame and locations through which threaded rods would pass through a mounting bracket allowing the gimbal frame skew angle to be rotated relative to the R-SAT deck.

This initial gimbal frame design was promising, but in the process of designing the mounting base the threaded rods which passed through it were determined to be unusable. Two attempts at designing the mounting base are shown in Figure 8.

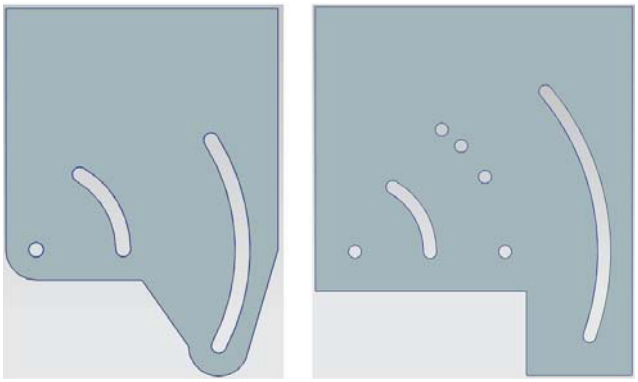

Figure 8. Early base mount concepts for skew angle adjustment

A full CAD model of the components at a skew angle of 90° shows promising results in Figure 9. However, at lower skew angles the mount base obstructs the momentum wheel gimbal movement, as shown in Figure 10. This obstruction led to yet another iteration of the gimbal frame design. The threaded rods were removed, and the side support curves were replaced with a new design which incorporated a pair of arcs as the inner and outer edges. These were aligned to a set of four rollers integrated into the base mount frame to allow the gimbal frame to be rotated through an infinite number of skew angles over a 130° range between 25° and 155°. This new structure also incorporated three holes in the side support frames which are used for quick indexing at the two most popular skew angles of 53.4° (or 116.6°) and 90°. The second gimbal frame CAD model is shown in Figure 11.

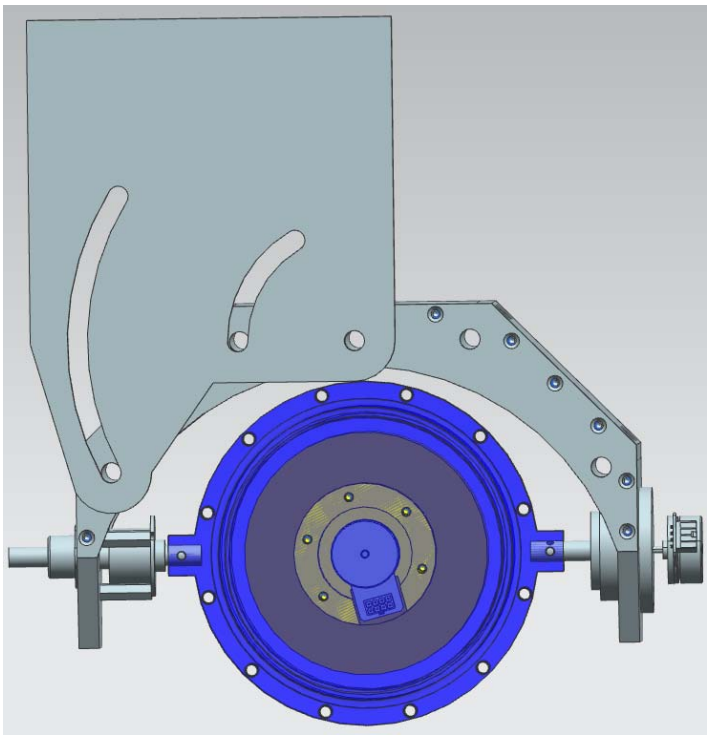

Figure 9. First gimbal frame and mount base prototype, 90° skew angle

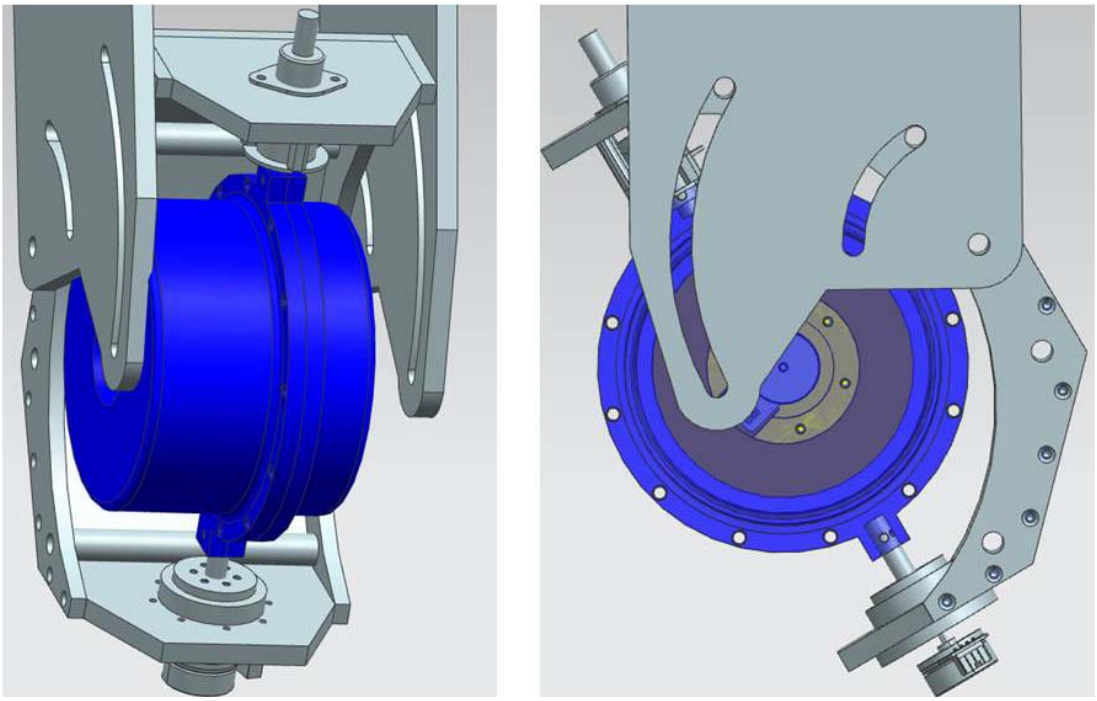

Figure 10. First gimbal frame and mount base prototype, 36.6° skew angle

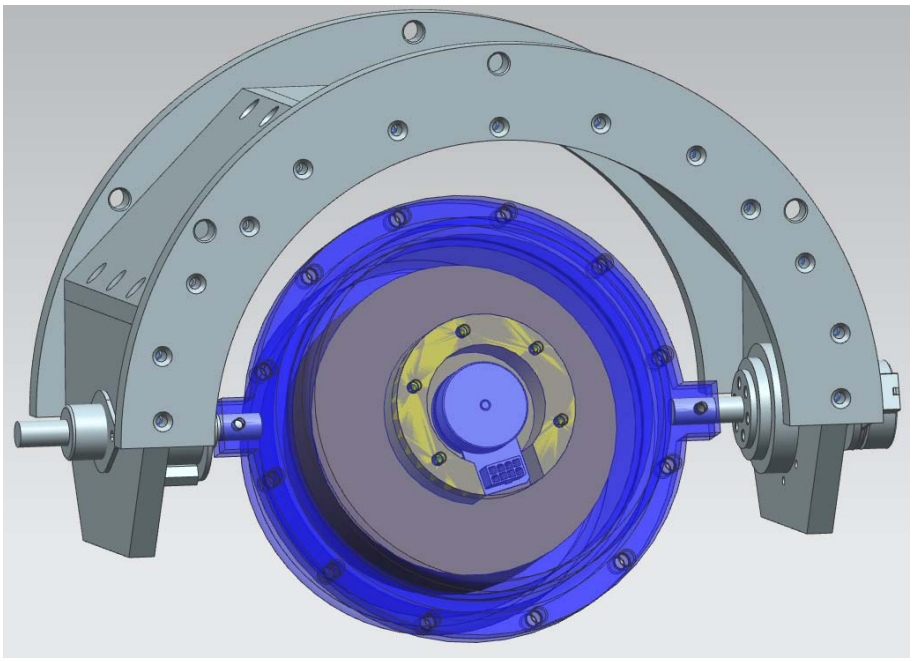

Figure 11. Second gimbal frame prototype

This new gimbal frame design was paired with a redesigned mount base which incorporated the rollers on which the gimbal frame could rotate as illustrated in the CAD model in Figure 12. This system uses rollers that are 1.905 cm (0.75 in) diameter and are stepped down and threaded to ½-13 on each end prior to passing through the mount base. The threaded ends are secured using flanged nylock nuts and it is the clamping force generated by the fasteners on these roller rods which secure the gimbal frame in its desired orientation. The three pin positions facilitate quick indexing, but the pins are not intended to be used to secure the gimbal frame position even in these three locations.

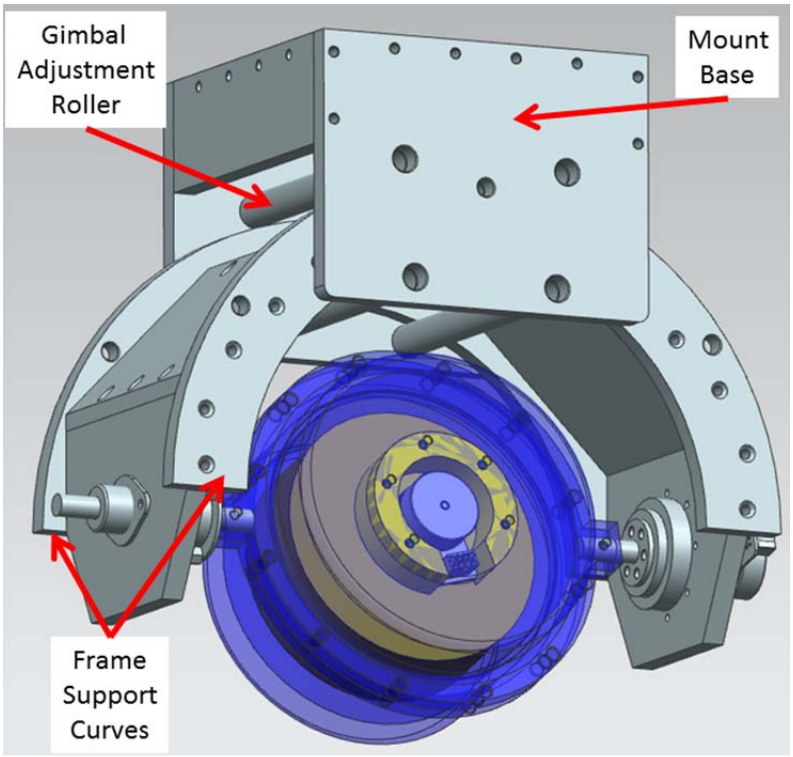

Figure 12. Second gimbal frame and mount base prototype

The design of the five flat plates, two curved supports for the gimbal frame, and the box shaped mount base with the four roller rods basically carried through all further design iterations with only minor modifications for improved operation and fit. The remaining modifications will be elaborated on in the prototyping section.

3. Gimbal Motor

While designing the gimbal frame, it was also necessary to determine the gimbal drive train components in order to properly specify the necessary clearances, mounting locations, mouting holes, and to identify any components which needed to pass through the structure. The first component of the drive train is the motor which causes the momentum wheel to rotate about the gimbal axis. Following on the Ackman work from [3], two Maxon Motor drives were selected for consideration. Both motors were built up from the EC45 flat brushless 50 Watt motor (PN 251601) [8], with additional Maxon Modular System components added on.

The Maxon EC45 was chosen for this application due to its relatively small size, suitable performance characteristics, commercial availability, and ease of integration as it is the same motor that was chosen to operate the Ackman momentum wheel. The commonality between the gimbal motor and the momentum wheel motor allows for the use of the same motor controller model for both motors. The drive electronics will be discussed in the Electrical System Design chapter. The performance parameters of the Maxon EC45 motor are listed in Table 4. The base version of this motor uses Hall sensors to determine the position and speed of the motor.

Table 4. Maxon EC45 performance parameters, from [8]

Supply Voltage	V	24
No Load Speed	rpm	6710
Maximum Speed	rpm	10000
Nominal Speed	rpm	5240
Nominal Torque	Nm	0.0834
Nominal Current	A	2.33
Stall Torque	Nm	0.780
Length	mm	21.3
Diameter/Width	mm	61.9

The first motor configuration, shown in Figure 13, included the addition of a planetary gearhead from the Maxon Modular System to the base EC45 motor. The gear ratio of the planetary gearhead allows for the motor to be operated in its optimal range (>1000 rpm). Below 1000 rpm the resolution of the Hall sensors makes speed regulation inaccurate. Although the planetary gearhead is a robust integrated solution, its use posed two primary challenges which made it non-ideal for this project. The first issue was related to the physical attachment of the motor assembly to the gimbal frame, and the rated radial load on the output shaft. The mounting points for this assembly are shown in the end on view of the motor in the left side image of Figure 13. These four M4 screws would have been responsible for supporting both the weight of the motor, as well as the weight of the momentum wheel cantilevered off of the opposite side.

The second issue with this motor was the output shaft dimensions. The Ackman wheel housing was designed with the same 12.7 mm (0.5 in) diameter gimbal shaft used

in the original Andrews wheel design. The 12mm (0.472 in) keyed output shaft could not be easily integrated into the momentum wheel design without additional shaft coupling components. Overall, the complexity of this solution, as well as the additional cost and reliability issues which are introduced with the increased parts count, made this motor a poor choice for this project.

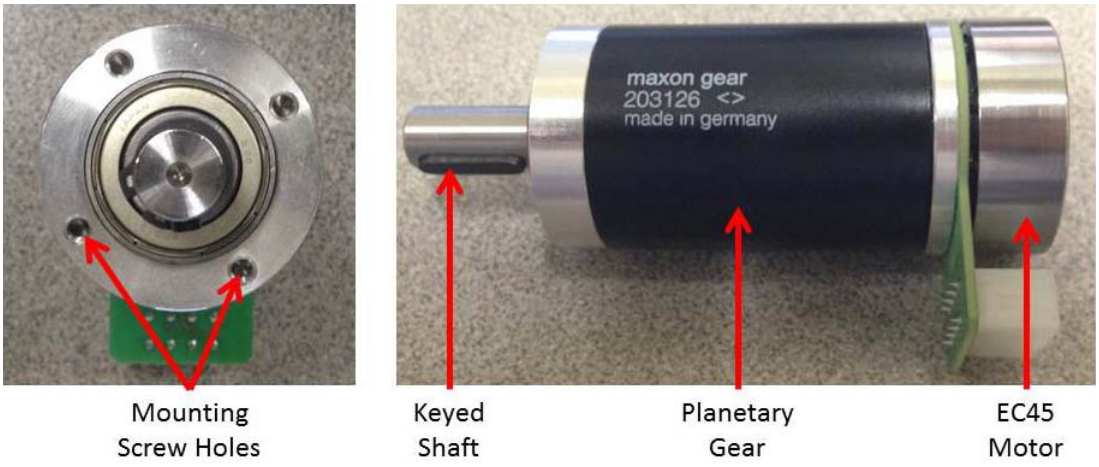

Figure 13. Maxon EC45 motor with planetary gearhead

The second motor configuration, shown in Figure 14, employs the same Maxon EC45 motor with an integrated encoder. This configuration proved to be an ideal choice for the gimbal motor. The small size of the motor was advantageous for keeping the overall frame design as compact as possible. Additionally, the incorporation of the encoder provided two separate advantages for this application. The first is that it provides greatly improved speed regulation for motor speeds lower than 1000 rpm. The second advantage is that the integrated encoder reduces the need for adding an absolute encoder on the gimbal shaft. The absolute encoder would provide greater gimbal position accuracy, but with the addition of a reduction gear in the drivetrain the accuracy and resolution of the integrated encoder may be sufficient.

The encoder which was chosen from the Maxon Modular system is the two channel, 1024 counts/revolution Maxon MILE encoder. The encoder will be further discussed in the Electrical System Design chapter.

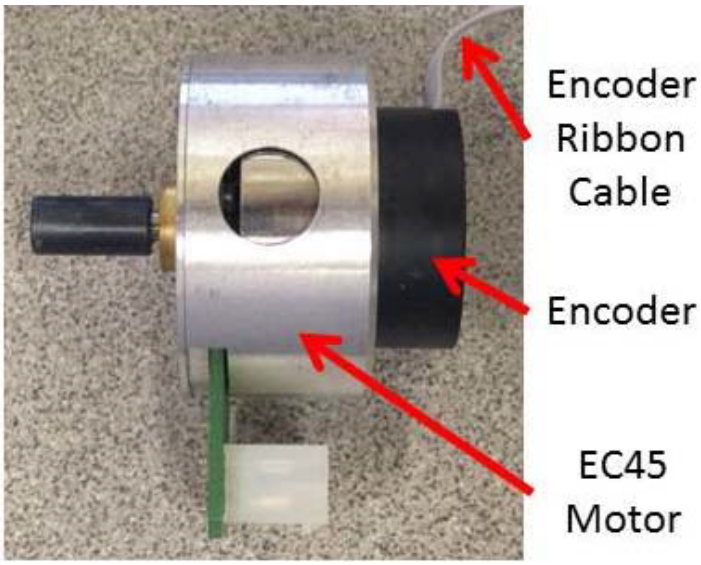

Figure 14. Maxon EC45 motor with encoder

4. Harmonic Drive

With the gimbal motor chosen, the next step was to determine how to connect the motor to the momentum wheel. Given that a typical CMG gimbal is operated over a range of 0 to 1 rad/s, motor speeds of 0 to 10 rpm are required for a direct drive design. These speeds are below the nominal operating range of the EC45 motor which was experimentally shown to be capable of rotating only as slowly as 25 rpm, even with the encoder providing the speed feedback. In order to operate the motor in a more optimal speed range a gear ratio of at least 100:1 was required.

After a review of several gear sets, the 100:1 gear ratio Harmonic Drive CSG-17–100, shown in Figure 15, used in the original Andrews design was chosen due to its exceptional performance, and compact design. Moreover, the harmonic drive has nearly zero backlash, which simplifies control of the gimbal axis. The hardware also allowed for mounting the drive through the vertical gimbal frame plate which provided both a more compact gimbal frame design, and a more robust mounting geometry for supporting the weight of the momentum wheel.

Figure 15. CSG-17–100 harmonic drive, from [9]

A harmonic drive is a strain wave gear composed primarily of three main components: a wave generator (input), a flexspline (output) and a fixed circular spline, as shown in the component set image in Figure 16.

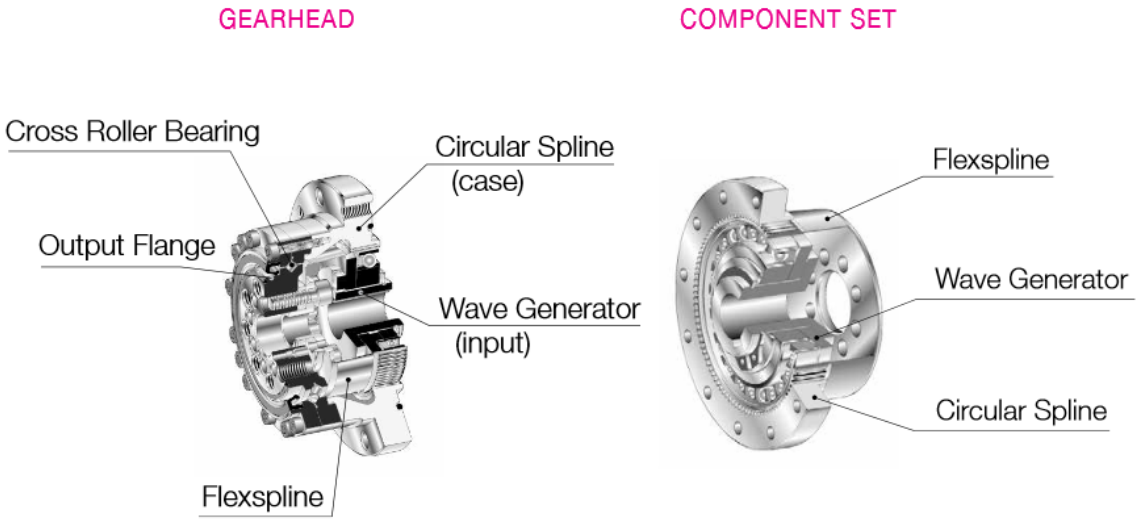

Figure 16. Cutaway view of harmonic drive, from [9]

Figure 17 provides a depiction of how these 3 components interact with each other throughout a full rotation of the input shaft. The shaft of the gimbal motor is connected to the elliptical wave generator to provide the high speed, low torque input to gimbal the momentum wheel. The wave generator itself consists of the elliptical base with a series of ball bearings that ride in a flexible race. The flexible race fits snugly

within the flexspline which flexes to conform to the elliptical shape of the wave generator. The motion of the flexspline is what provides the unique performance characteristics of this gearing technology. In a harmonic drive up to 30% of the gear teeth are engaged at any given time which reduces the force on each individual tooth while enabling high torque transfer through the system. The CSG-17–100 has a circular spline with 202 teeth, and a flexspline with 200 teeth which means that approximately 60 teeth on each spline are engaged at any one time. In contrast, the more commonly used spur gear reducer (shown in Figure 18) often only has 1 or 2 teeth engaged at a time which imparts a high force load on each of those teeth. This high load per tooth is also common across other gearing types including worm gears, planetary drives, helical gears, etc. Although the force that would be applied to the gear tooth by the gimbal motor would not be extreme, the larger issue associated with this single tooth engagement is the effect of backlash [3] . During spacecraft maneuvers and while maintaining a spacecraft pointing orientation the gimbal motor may frequently have to change directions to apply small torque corrections. This motion can cause accelerated wear on the gear teeth, and the backlash makes fine control of the spacecraft attitude more difficult. In the design of a CMG for a terrestrial testbed this operation must be taken into account due to the testbed ADCS having to correct for additional perturbations due to gravity and aerodynamic effects.

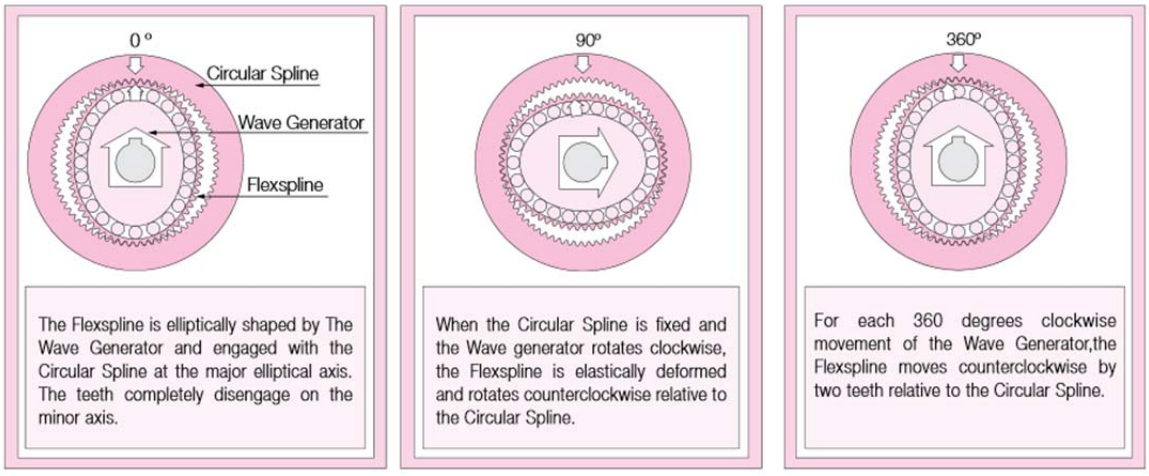

Figure 17. Illustration of harmonic drive operation, from [9]

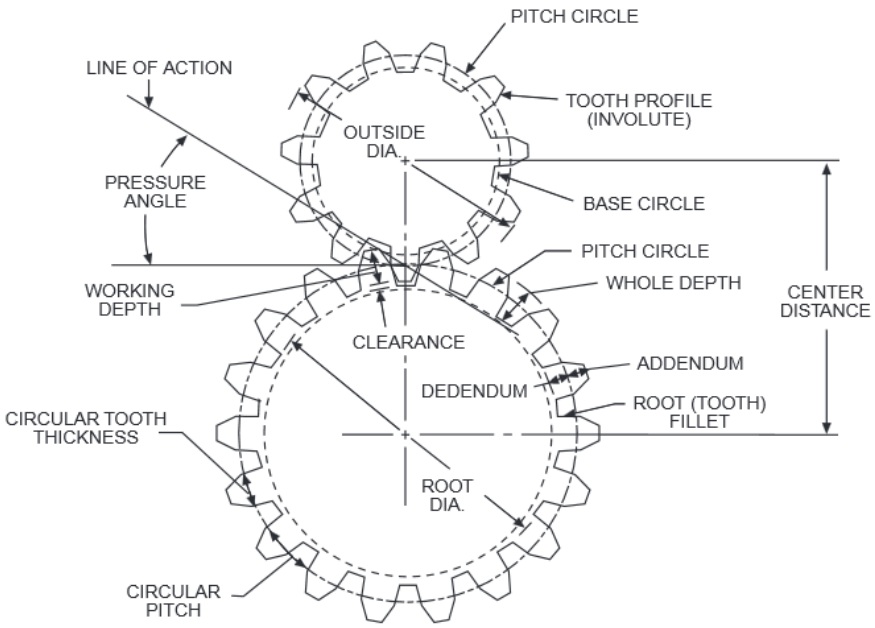

Figure 18. Spur gear reducer, from [10]

In addition to the number of teeth that are engaged, the specific type of motion that harmonic drive teeth exhibit is unique as well. In the more traditional gearing technologies, such as spur gears, the gear teeth undergo a sliding motion where only one side of the gear tooth is engaged with the corresponding tooth of the opposing cog. The sliding motion and concentrated pressure on a small area of the gear tooth leads to wear and a need to construct strong gear teeth. In the harmonic drive, the gears do not slide across each other as the input and output shafts rotate. Instead, the flexspline gears move in and out of the gear slots in the circular spline at an angle normal to the center of the circular spline. This operation provides a 90° pressure angle and a line of motion which radiates directly from the center of the harmonic drive.

The actual rotational motion of the output shaft, which is connected to the flexspline, is caused by the fact that the flexspline has 2 teeth less than the circular spline has. This difference in the number of gear teeth causes the flexspline to “walk” around the circular spline, and provides the gear ratio as calculated in Equation (8). For the specific drive used here, the result of the calculation is -100 which means that the gear ratio is 100:1 and that the direction of motion of the output shaft is opposite that of the input shaft.

$$N_g = \frac{n_{flex\_spline}}{\left(n_{flex\_spline} - n_{circular\_spline}\right)} \tag{8}$$

5. Gimbal Bearing

In conjunction with the harmonic drive supporting one end of the momentum wheel within the frame, and in order to allow for the gimbal axis to rotate, a pair of cylindrical shafts was attached to opposite sides of the wheel housing. On the harmonic drive side, a flanged shaft was bolted to the flexspline base, as shown in Figure 19. On the opposite side a simple shaft with shoulder, as shown in Figure 20, was attached. This shaft passes through a bearing which supports the shaft both radially and axially.

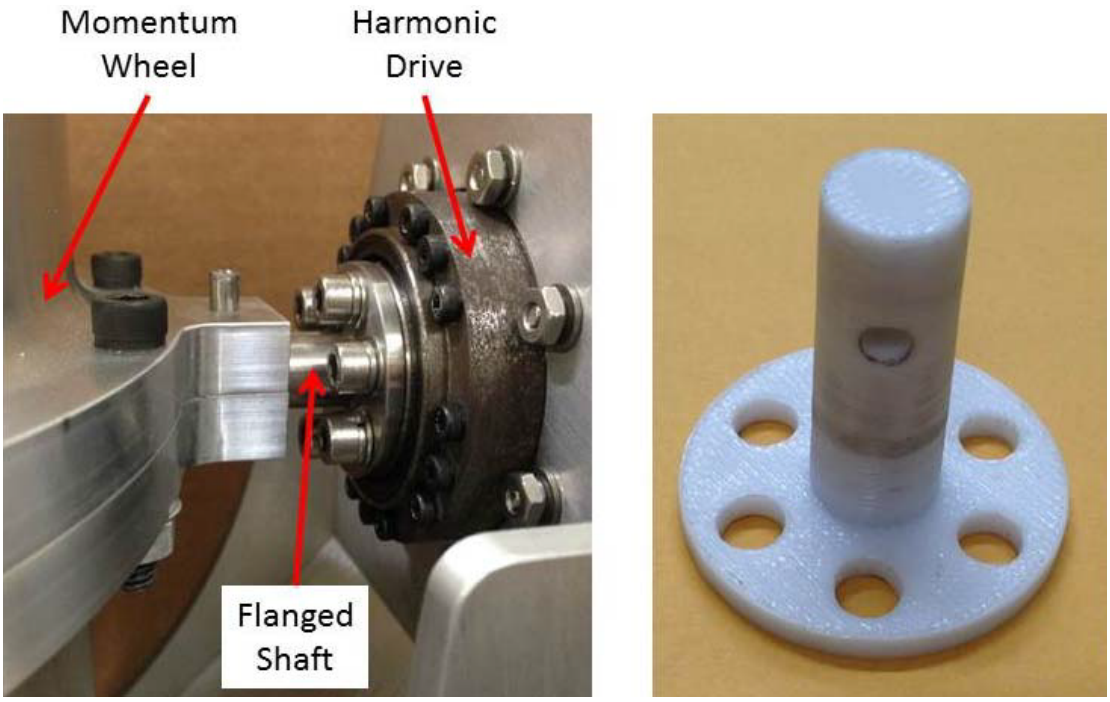

Figure 19. Drive side gimbal shaft, (left) mounted in CMG, (right) 3D printed prototype

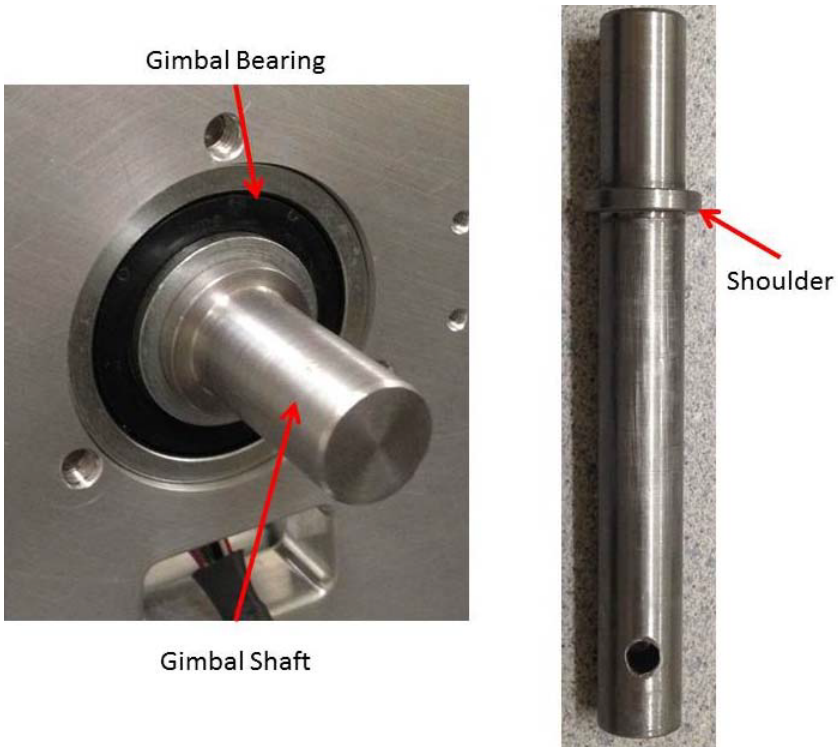

Figure 20. Bearing side gimbal shaft, (left) installed in CMG, (right) pre-installed

The first two system prototypes made use of the roller needle bearing which was used in the Andrews design. In an effort to reduce the overall size of the CMG frame, and provide smoother operation a sealed roller ball bearing with a 12.7 mm (0.5 in) thickness, equal to the thickness of the frame plate which it mounts inside, was selected as shown in Figure 21. This bearing also incorporates a small shoulder around its circumference on one side of the bearing which fits snugly into a counterbore designed into the gimbal frame. This allows for the bearing to be firmly mounted in the frame and a shoulder machined into the gimbal shaft provides further insurance that the bearing will not be able to work its way out of position. The sealed ball bearing can also absorb some of the axial load on the shaft that arises due to the weight of the momentum wheel in orientations where the skew angle is not 90°. The needle bearing used in the original Andrews design cannot support any axial load, which placed additional stress on the harmonic drive components.

Figure 21. Gimbal shaft sealed roller ball bearing (HEIM RF82214PP)

D. SUMMARY

The structural design of the CMG provided a continuous, manually adjustable skew angle which allows for reconfiguration of the CMG array on the R-SAT testbed. With a focus on making the design as compact as possible, while being easy to maintain and upgrade, the design consisted of the gimbal frame consisting of five aluminum plates bolted together at 45° angles to form a "U" shape, and a pair of curved supports were attached to the sides to both provide structural rigidity and to facilitate the skew angle adjustability.

THIS PAGE INTENTIONALLY LEFT BLANK

III. ELECTRICAL SYSTEM DESIGN

A. INTRODUCTION

Although critical to the operation of the CMG, the mechanical system design was much more straightforward than the electrical system design, and took far less time to complete. While the mechanical system took approximately 3 months to design from the first iteration to the final design, the electrical and electronic control systems took more than twice the effort to get an operational system that could be used for characterization testing. This increase in time was not in the design of the CMG electronics, but in the communications necessary to command the CMG wirelessly on the testbed.

The final electrical system which was used for system testing consisted of two separate power supplies, one at 24 VDC and the other at 5 VDC, as well as two Maxon DC motors, two Maxon EPOS2 motor controllers, a BeagleBone Black (BBB) single board computer (SBC) running Linux Debian, a SparkFun Razor 9-DOF inertial measurement unit (IMU), and a USB hub with an IEEE802.11b/g/n USB Wi-Fi adapter.

B. ELECTRICAL POWER

The electrical system design can be divided into two separate subsystems with the first being the electrical power distribution system, and the second being the electronic components which use that electrical power. The electrical power system is comprised of two separate DC busses, one at 24 VDC and the second at 5 VDC. In order to allow for wireless operation of the CMG on an air bearing testbed this DC power was supplied by onboard batteries.

1. 24 VDC Bus

The motor control power bus for the test system is 24 VDC supplied by a single DEWALT 24V XR+ NiCd battery. The battery was mounted to a custom designed power supply block with an on/off switch for safe installation and removal of the battery pack and connectors for standard banana plugs. The battery and block are shown in Figure 22.

The 24 VDC bus powers the two EPOS2 motor controllers, and the battery was capable of providing 3–6 hours of run time while powering both the gimbal and momentum wheel motors. During high gimbal rate operations of 1 rad/s and a momentum wheel speed of 5000 rpm, the battery could provide approximately 8A at 24 VDC during transients, with an average current draw closer to 5A. The power usage details will be discussed further in the System Characterization chapter.

Figure 22. DEWALT 24 V battery pack and power supply block

2. 5 VDC Bus

The 5 VDC powers the onboard BBB flight computer, and all of the USB components. The power is supplied by an Anker 12000 mAh, 5 VDC battery pack, shown in Figure 23, which can supply up to 4A from each of its three female USB-A output ports. The high energy capacity of this battery supported multiple days of testing on a single charge.

Figure 23. Anker 5 V battery pack, from [11]

Only two of the output ports were needed to power all of the system components. The BBB SBC was powered from one port via a USB-A to USB mini-B connector cable, and a D-Link four-port USB hub was powered from the second port via a custom USB-A to DC barrel connector. Early attempts were made to supply the 5 VDC power through a regulator on the 24 VDC bus, but due to the relatively high current draw of some components (greater than 1A each for the BBB during startup and the USB Wi-Fi adapter), a suitable regulator was not readily available. The use of the 5 VDC battery also allowed for isolation of the high power draw 24 VDC bus and the lower power 5 VDC bus which allowed for more consistent power delivery to the low voltage devices. To eliminate the need for the additional battery pack in the future, a suitable 5 V regulator circuit needs to be constructed.

C. MOTOR CONTROLLERS

One idea that was incorporated into this open-architecture CMG was a desire to use as many common components as possible to reduce overall system complexity. A primary instance of this was the selection of the motor controllers which power and control the momentum wheel motor and the gimbal motor. As discussed in the mechanical design chapter, both of these motors are Maxon EC45 drives. The only difference between the two is that the gimbal motor has an integrated encoder while the momentum wheel motor does not. The commonality of these two motors allowed for the

use of an identical Maxon EPOS2 24/5 motor controller for each motor. This controller has a great deal of flexibility as it can be connected to the controlling PC via RS232 serial connection or USB, and it also supports a CAN bus architecture. Although not used during this portion of the R-SAT CMG system design, the CAN architecture built into these controllers was one of the attractive features which led to their use. The long term plan for the control of the R-SAT with all four CMGs integrated into the ADCS is to have the motor controllers and system sensors all connected via a CAN architecture.

For this phase the CAN bus was not implemented, and instead the gimbal motor was connected to the EPOS2, and subsequently to the BBB flight computer using USB, as shown in Figure 24. The BBB is depicted as the PC in this image.

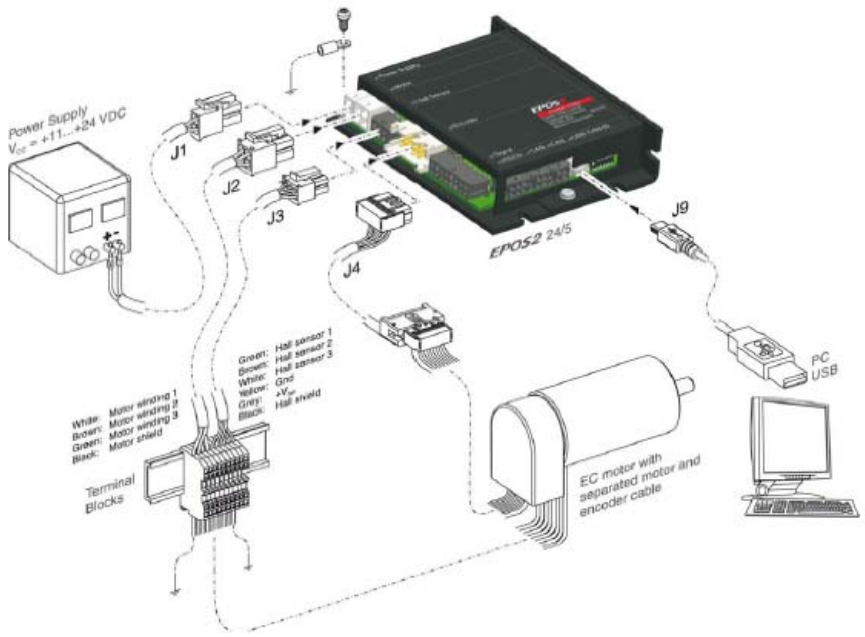

Figure 24. Gimbal motor wiring schematic, from [12]

The momentum wheel motor controller was connected in a very similar fashion, as shown in Figure 25. The only difference is that there is no encoder connection to the EPOS2 for the momentum wheel motor.

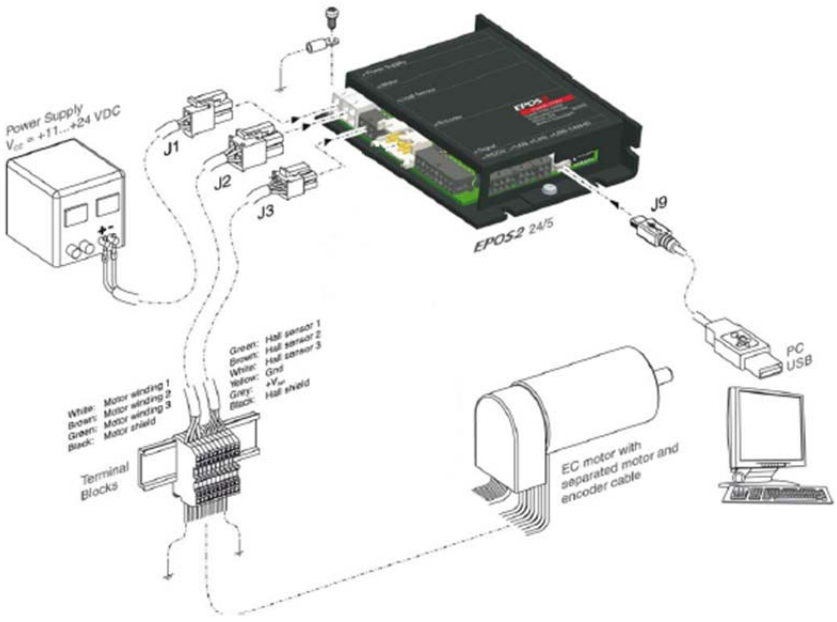

Figure 25. Momentum wheel motor wiring schematic, after [12]

D. SENSORS

In the design of many control systems, it is crucial to receive feedback from a series of sensors in order to close the loop. In the design of the CMG control system and the rudimentary ADCS associated with the 1-DOF testbed used for characterization testing, a series of sensors was used to achieve proper system operation and to provide performance data for post test processing. The sensors that were used for the closed loop operation of the CMG were the Hall effect sensors resident within the Maxon EC45 motors, and the optical encoder which was integrated as part of the gimbal motor. These two sensors provided motor rate and position feedback used both for motor control and for data collection related to the performance during testing. One additional sensor, an IMU, was included in the testbed to provide platform data for post test analysis. The IMU was not used to provide feedback to the motor controllers. When fully integrated into the upgraded R-SAT the IMU data will, however, be used in the ADCS feedback loop.

1. Motor Hall Sensor

The Maxon EC45 motors use Hall effect sensors as the baseline means of measuring motor position and velocity. The measurements are fed to the PD controller in

the EPOS2 motor controller to adjust the speed of the motor. A Hall sensor is essentially a proximity switch on which a voltage is induced when a magnet is passed by the sensor. It is this proximity switching, and the use of multiple sensors at fixed angular distances from one another that allows for motor position measurement. The EC45 motor utilizes three sensors, spaced 120° apart. Due to the ability to measure the linear voltage changes as the magnet moves closer to the sensor, the measured position accuracy is better than if the sensor acted as a digital switch. The performance of the EC45 Hall sensors provides position accuracy of approximately 70°. This level of accuracy is sufficient when providing velocity feedback for a motor that is spinning at 5000 rpm like the momentum wheel motor, but at speeds below 1000 rpm this position resolution makes motor speed control very difficult and inaccurate. Due to this low speed motor control issue, the Hall sensors are not an ideal choice for control of the gimbal motor. For that application, an integrated optical encoder is used instead.

2. Motor Encoder

As previously mentioned, the Maxon EC45 gimbal motor utilizes an integrated Maxon MILE encoder to measure motor position and rate. The encoder is a two channel, 1024 count/revolution design. The use of two channels allows for 90° phase measurements from the digital counts as shown in Figure 26. This phase difference between the two channels allows for four distinct measurements to be taken per encoder count. This quadrature counting technique increases the resolution of the encoder by a factor of four resulting in 4096 counts/revolution. This increased position resolution, when compared to the Hall effect sensors, provides two distinct benefits when used for the gimbal motor.

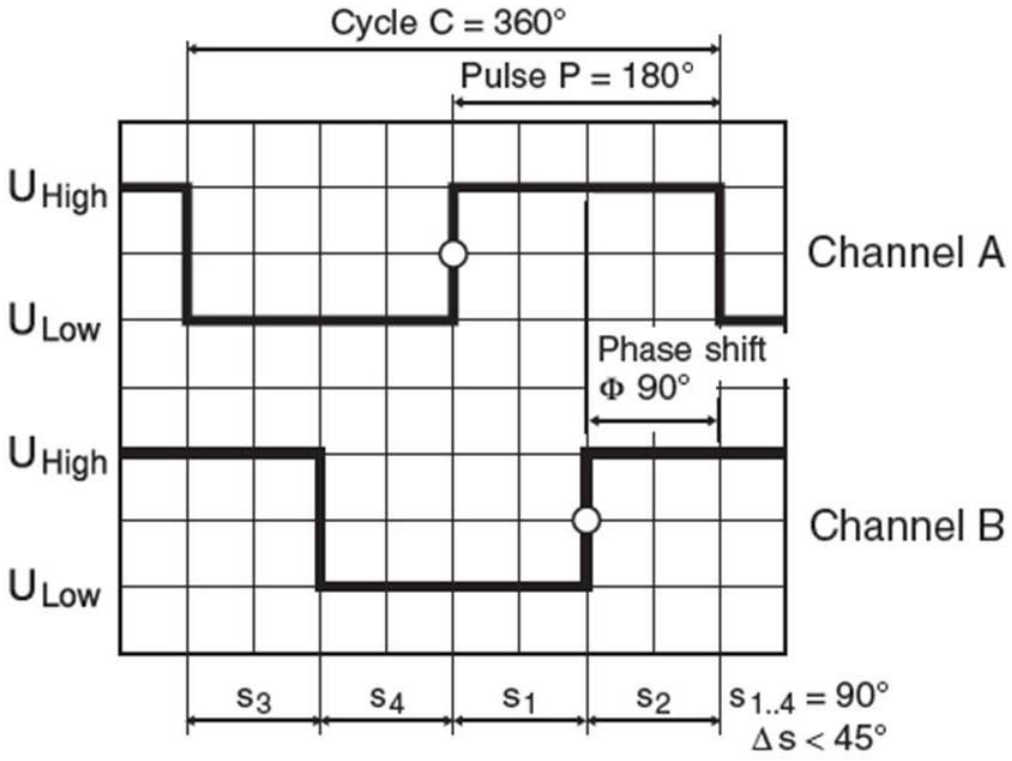

Figure 26. Two-channel encoder quadrature counting, after [8]

The first benefit is that the 4096 quadrature counts per revolution equate to a motor position resolution of 8.79 x 10^{-2} degrees (1.53 x 10^{-3} radians). This greatly improves the speed control of the motor at low speeds, especially below 1000 rpm where the Hall effect sensors are inadequate. Even with the 100:1 harmonic drive gear ratio, the gimbal motor speed for the maximum gimbal rate of 1 rad/s is 955 rpm, below the range where Hall sensors can be used reliably. In addition to the motor control problem, is the fact that CMGs require precise gimbal rate control and knowledge of the gimbal position for proper ADCS operation.

The second benefit is that with the addition of the 100:1 harmonic drive reduction gear the encoder counts for a single revolution of the gimbal shaft increase to 409,600 encoder counts. This provides a gimbal position resolution of 8.89 x 10^{-4} degrees/count, or 1.53 x 10^{-5} radians/count, which allows for the use of the motor encoder as the primary means of gimbal shaft position measurement vice needing a separate absolute encoder for the gimbal shaft. A first order analysis of the integrated motor encoder

performance with the harmonic drive gearing indicates that gimbal position can be determined with 3.20 arc second accuracy which actually exceeds the 36 arc second performance of the Dynapar AI25 absolute encoder selected for gimbal position measurement in [3]. Even the harmonic drive backlash, rated at 2.83 x 10^{-3} degrees which equates to 1/30th of the resolution of the motor encoder (8.79 x 10^{-2} degrees), seems to be an insignificant factor in the overall accuracy of measuring the gimbal shaft position. When building the final set of 4 CMGs for incorporation onto the next generation R-SAT, a more in-depth evaluation of the gimbal position accuracy will be necessary in order to decide whether to use the system as-is, or to add an absolute encoder as suggested in [3]. One area of concern for use in an ADCS is that the motor encoder measures relative position from an initial position registered when the encoder is powered on whereas an absolute encoder always provides position data relative to a given user selected datum.

3. Inertial Measurement Unit

In keeping with the desire to reduce the cost of the CMG and the testbed as low as possible, an inexpensive IMU was chosen for measuring the test platform position, rate of movement, and acceleration. In conjunction with concurrent research being conducted at NPS [13] that used the Sparkfun Razor 9-DOF IMU [14] for high precision measurement, the same unit was chosen to be integrated into the test platform for this project. This IMU, shown in Figure 27, uses three sensors in a 2.79 cm x 4.06 cm (1.1in x 1.6 in) package to provide the 9-DOF measurements. The three sensors are a MEMS triple-axis gyro (ITG-3200) [15], a triple-axis accelerometer (ADXL345) [16] and a triple-axis magnetometer (HMC5883L) [17]. The serial output from this board was routed through a SparkFun USB to Serial Breakout (FT232RL) board, and out to the onboard computer via the USB hub, shown in Figure 28. The performance of the IMU will be discussed later in the System Characterization chapter.

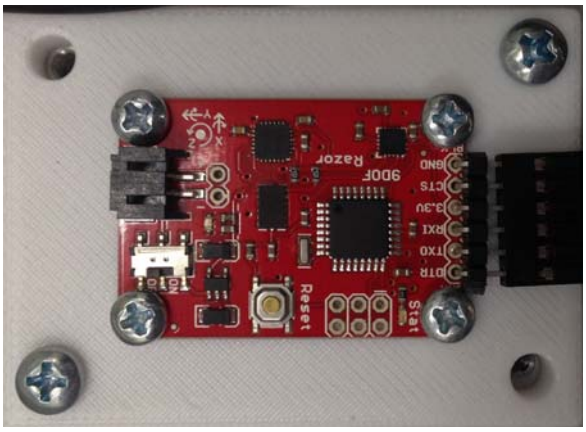

Figure 27. Razor 9-DOF IMU

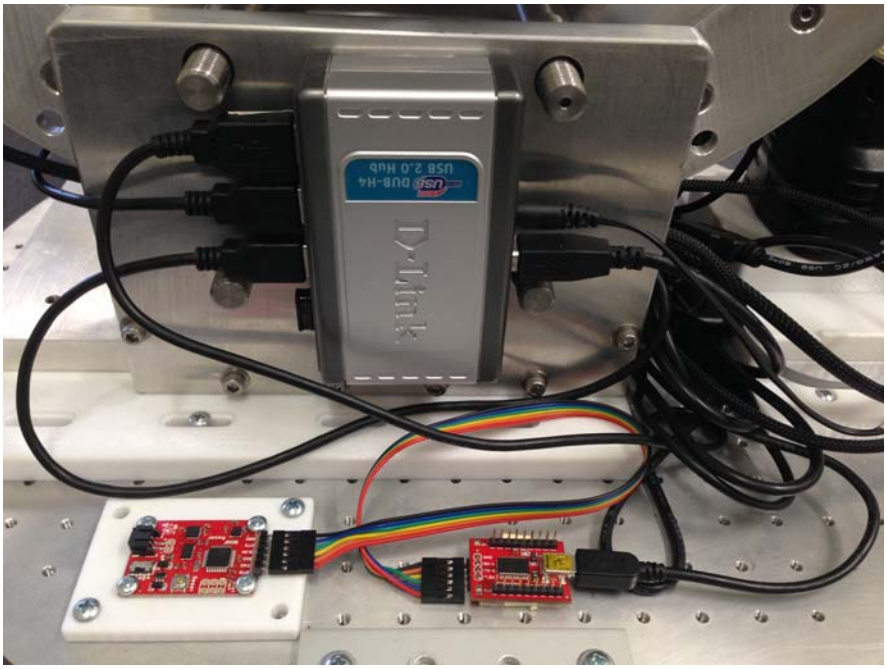

Figure 28. IMU to SBC interface

E. SLIP RING

In order to provide electrical power to, and to receive data from, the momentum wheel motor a slip ring on the gimbal shaft was necessary. After reviewing the number of connections necessary to receive the Hall sensor data and provide the necessary electrical power to the motor, a MOOG twelve wire slip ring, shown in Figure 29, was chosen.

Figure 29. MOOG slip ring, from [18]

The limiting factor for the slip ring was the electrical current which needed to be supplied to the motor. The slip ring is rated to handle up to 2A per ring, and the Maxon EC45 motors are rated to a maximum instantaneous motor current of 4.6A with a maximum sustained current of 2.4A. At these load levels, and with the power to the motor supplied via the 3 phase motor connections it was determined that each of the 3 motor supply pins would utilize parallel wiring paths through the slip ring, using 2 rings per motor connection. This led to using 6 wires for motor power, and 5 wires for the 5 Hall sensor pins. The remaining wire was unused and terminated on both ends.

F. ONBOARD COMPUTER

After a number of failed attempts to wirelessly interface with the EPOS2 motor controllers directly from a PC, the decision was made to incorporate an onboard computer into the air bearing testbed to issue the commands to the controllers. The BeagleBone Black SBC, shown in Figure 30, was selected for this task. This small, low cost Linux-based computer interfaced, via its USB connection, to the D-Link four-port USB hub allowing it to control and receive data from multiple controllers and sensors simultaneously. The BBB was powered by a male USB-A to male USB mini-B connector from the 5 VDC bus.

The BBB is designed to be very flexible with rows of breakout connectors for controlling peripheral devices, sending and receiving serial communications and powering external devices. It also provides a USB-A connector, a 10/100 LAN connector and a micro-HDMI video connector.

Figure 30. BeagleBone Black single board computer

1. Software

The BBB can run a number of different operating systems, and for this project the BBB was flashed with the Debian release of Linux [19]. This operating system was chosen for its open source underpinnings, and the fact that it was already tested and built for the BBB. The BBB was loaded with the EPOS2 Linux source code provided by Maxon Motors. The source code was compiled for use on the BBB ARM processor, and the C libraries were built to support operations. The actual control software for the system was built as a Python 2.7 wrapper which routed calls to the Maxon C control code, and a GUI was developed using PyQt which allowed for real-time monitoring of the CMG during operations.

The GUI was designed as a four window screen, shown in Figure 31, with the following layout. The top left window was dedicated to monitoring the speed, and current draw for the momentum wheel motor. Unlike the other three GUI windows, the "Rotor Velocity and Current" window displayed the most recent 720 seconds of operations to allow for monitoring of any operating trends such as a reduction in motor speed due to battery voltage dipping, or to see if the current consumption was increasing or decreasing in ways that would not be expected for the given test parameters. For this window the longer time horizon allowed for enhanced trend monitoring with a reduction in the resolution of near term operations. The other three windows each had 120 second time scales, as the long term trending was less important, and the real-time resolution was vital to the conduct of tests. The bottom left window showed the angular position and

acceleration of the testbed platform from the Razor 9-DOF IMU. The two windows on the right side were used to monitor the gimbal motor speed and current draw, and the gimbal shaft angle. The GUI was not used for post test data review as its purpose was to provide a real-time view of the system with primary emphasis on motor speeds, motor current, and gimbal position to provide early indication if something was malfunctioning. This real-time monitoring prevented test runs from going on for tens of minutes to hours before the test operator would see that a failure had taken place, or that hardware was malfunctioning in a way that may cause damage to components. It also provided the only feedback on momentum wheel speed, which is vital to proper CMG operation, and is the only means to identify if the 24 V battery needed recharged, prior to its voltage dipping low enough that the controllers would power off.

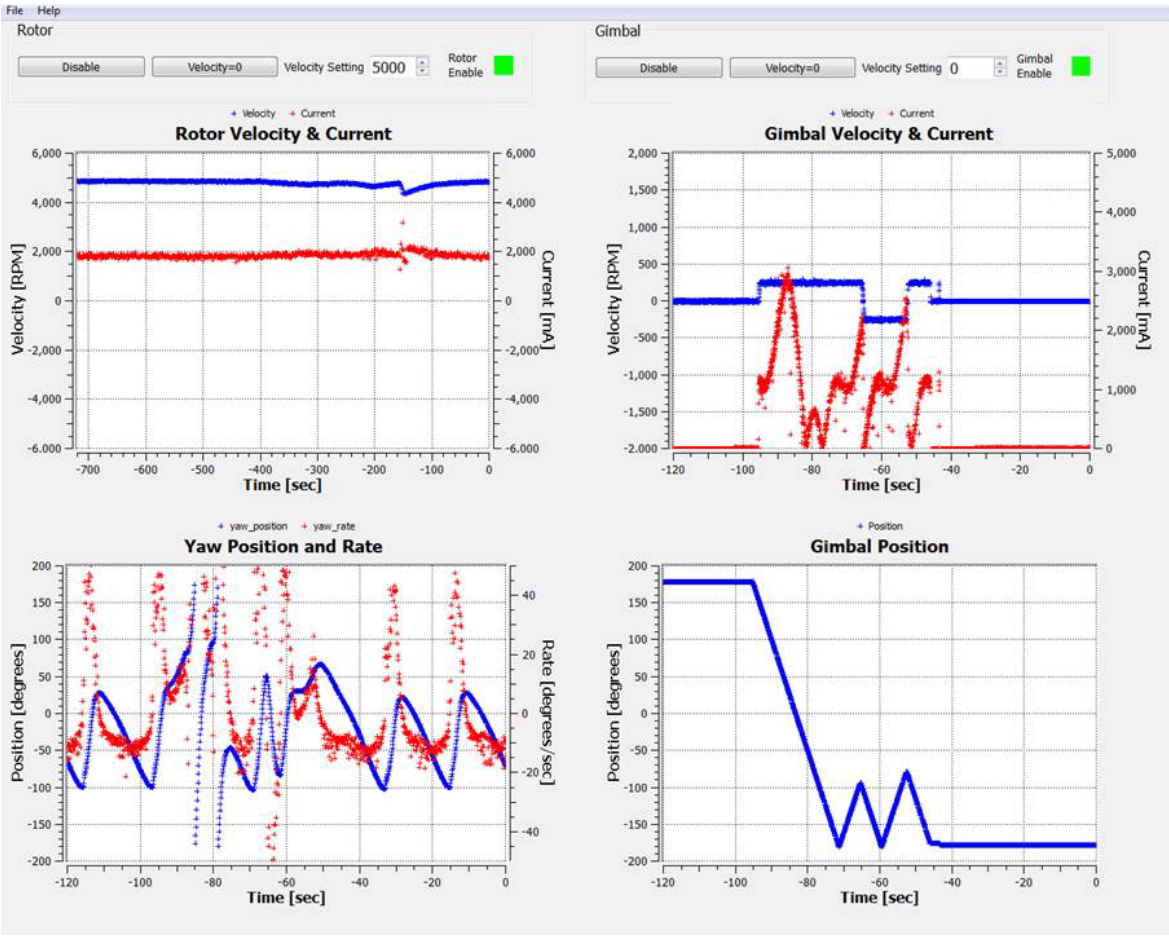

Figure 31. Real-time performance monitoring GUI

The operation of the BBB was controlled from a Windows 7 laptop via a secure shell (SSH) connection over the campus Wi-Fi network. A copy of the Python code was resident on both the laptop and the BBB. The local laptop Python code was used for the real-time monitoring of system parameters to reduce the data which needed to be sent from the BBB to the PC. The actual control of the motor controllers was performed via the Python code on the BBB which was remotely commanded from the PC via the SSH connection. All commands were issued from the PC, and the collected system data was streamed directly to the PC for storage due to the limited remaining storage capacity onboard the BBB.

G. COMMUNICATION PROTOCOLS

During the integration of the CMG to the testbed, multiple attempts were made to control the EPOS2 motor controllers using different wireless serial connectivity protocols including Bluetooth and X-Bee (IEEE 802.16) radios. Although successful loopback tests were conducted using both of these protocols, a timing issue (which was never resolved), existed between the EPOS2 and the wireless devices. The failure to interface directly with the motor controllers led to the implementation of the BBB onboard computer.

1. USB

As discussed in the Onboard Computer section of this chapter the BBB has a number of available I/O options, including serial and USB communication protocols. During early discussions on how to handle this data connectivity a preference for using serial communications was established. An investigation into using the EPOS2 motor controllers via serial connections identified that these controllers are specifically designed for industrial applications. In order to meet the demands of the industrial environment, the RS232 standard which is used for serial connectivity requires a higher voltage than the TTL signals most computing systems provide. The RS232 standard allows for a wide range of logic levels, and the EPOS2 controller therefore operates at a 9 V logic level. Most of the low power components which were being used to communicate with the controller were only capable of providing logic levels of 3.3 to 5 V. RS232 connectivity could have been used with the addition of logic level shifters, but the added complexity

made the USB communication protocol a more attractive option. A four port D-Link USB (shown previously in Figure 28) handled the routing of the USB traffic between the BBB and the system devices as listed in Table 5.

Table 5. USB hub port mapping

Port	Device
1	IMU
2	Gimbal controller (EPOS2)
3	Momentum Wheel controller (EPOS2)
4	EDIMAX WiFi Adapter

The D-Link USB hub was powered from the 5 V bus. An attempt was made in early testbed design to use an unpowered USB hub, but the current draw of the WiFi adapter exceeded the power that could be provided by the BBB USB port.

2. Wi-Fi

One major advantage to using the BBB onboard computer was the possibility of using the campus IEEE 802.11 WiFi network to communicate between the controlling PC and the onboard computer. This connectivity was provided by the EDIMAX Wireless IEEE802.11 b/g/n nano USB adapter, shown in Figure 32. The low cost, 150 Mbps data rates, commercial availability, and small form factor made this an ideal choice for this project. The unit was fully compatible with Linux operating systems and integrated easily with the CMG system.

Figure 32. EDIMAX Wireless IEEE802.11b/g/n nano USB adapter, from [20]

H. SUMMARY

The electrical system for the integrated CMG and testbed consisted of an electrical power distribution system, and an interconnected system of computers, controllers, and sensors. The power distribution was split across a 24 VDC bus and a 5 VDC bus powered by a 24 V DEWALT NiCd battery and a 5 V Anker USB battery, respectively. The 24 VDC bus provided the electrical power for the two EPOS2 24/5 motor controllers used to operate the momentum wheel and gimbal motors. The 5 VDC bus powered the BBB onboard computer, EDIMAX WiFi adapter, D-Link USB hub, and Sparkfun Razor IMU. The dual battery system construct allowed for three to six hours of constant testing on the 24 V battery, and multiple days of operations on a single charge of the 5 V source.

THIS PAGE INTENTIONALLY LEFT BLANK

IV. RAPID PROTOTYPING

A. INTRODUCTION

Rapid prototyping of system components using a 3D printer has become an integral part of the system design process for countless products in recent years. The design of this CMG benefitted significantly from the availability of this technology at NPS. A Fortus 300mc rapid prototyping machine which utilizes fused deposition modeling (FDM) to construct 3 dimensional parts through an additive fabrication process was used. The 3D printer utilized reels of white polycarbonate structural material and break-away support system (BASS) material. The polycarbonate material composed the structure of the components which were printed and the BASS was used in the printing process as a support material which reinforced subsequent printing layers in areas such as counter bored holes, channels designed into the structure, etc. The BASS material was removed and discarded after printing.

The prototyping of the system components for fit and functional testing was not the only use of a 3D printer. In fact, it could be argued that during the execution of this project the use of the 3D printer for prototyping the gimbal frame was less important than its use for fabricating custom end-use components which were integrated as part of the testbed used to characterize the CMG. A number of components were designed and produced for use on the testbed, some of which would have been prohibitively expensive to machine from aluminum or other materials. This chapter will discuss the use of the NPS 3D printer for both the prototyping of the CMG components, and also for the fabrication of vital testbed hardware.

B. CMG FRAME RAPID PROTOTYPING

A major factor in the design of this CMG was the process of iterative CAD design coupled with rapid prototyping using the 3D printer to print out full scale models of the design. These prototyped components were used to physically evaluate the design and conduct fit checks to ensure compliance with the design requirements. The first few weeks of the design effort were spent evaluating the existing Andrews Space frame

design, taking measurements of components, and assessing which components could be reused. Prototype designs were modeled in the NX 8.5 CAD software suite. After a number of iterations and simulated fit checks in the CAD software, a design was converted to a stereo lithography (.stl) file and then sent to the 3D printer for rapid prototyping. The first batch of 3D printed materials for the first gimbal frame prototype is shown in Figure 33. After the printing of two separate batches of parts, the first prototype was constructed as shown in Figure 34.

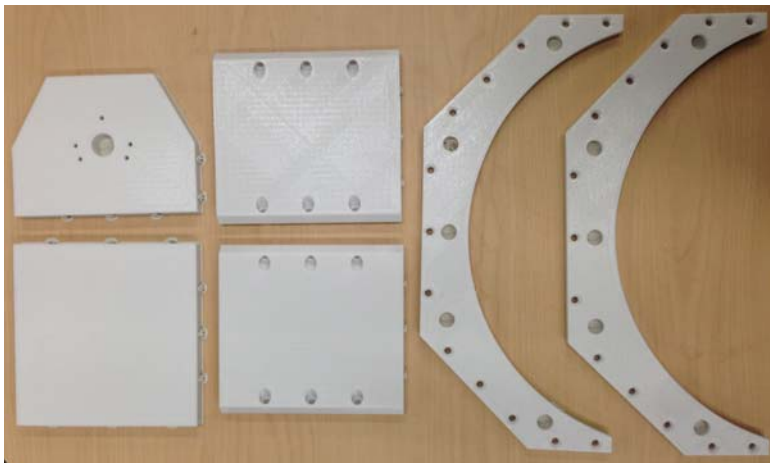

Figure 33. First batch of 3D printed prototype parts

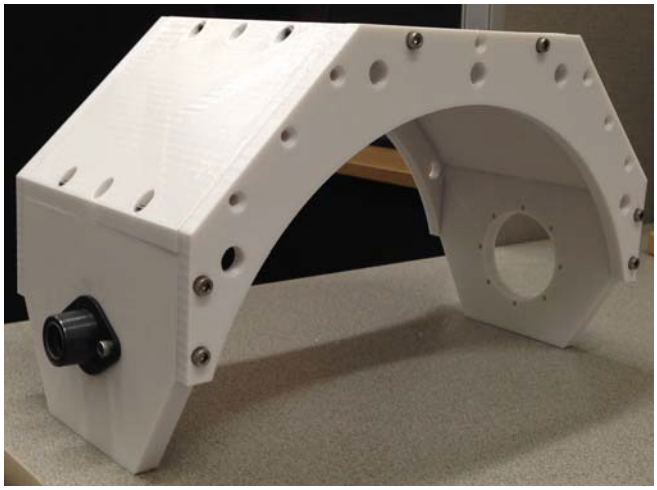

Figure 34. First gimbal frame prototype (assembled)

As discussed in the Mechanical System Design chapter, this first iteration possessed a number of design shortfalls in the initial gimbal angle adjustment mechanism that were identified in the CAD model and redesigned. This effort took place while the components of the first prototype were in the 3D printer. The new side support plates were sent to the printer and the second gimbal frame prototype was built, as shown in Figure 35. With the exception of the new side plates all of the previously printed components could be reused.

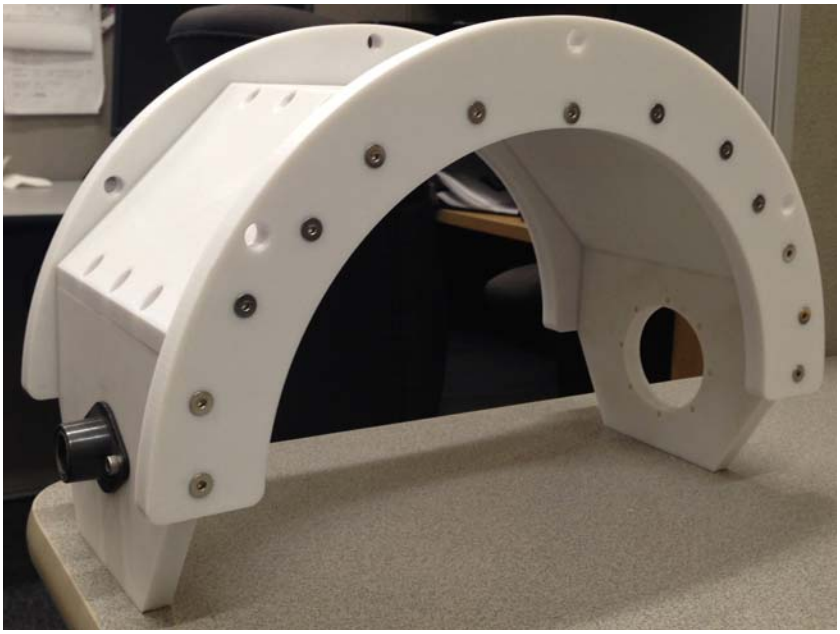

Figure 35. Second gimbal frame prototype (assembled)

When designing and building a single system in the CAD environment it is difficult to get a feel for the relative dimensions of the object. Throughout the iterations on the design which led up to the first, and even second prototype, the width of the plates and the thickness of the curved support structure were significantly oversized. Once the model was constructed it became apparent that it could be reduced in dimension, while still providing sufficient stiffness.

The width of each of the five flat plates was reduced from 15.24 cm (6 in) to 12.7 cm (5 in), and the thickness of the curved support plates was reduced from 1.27 cm (0.5 in) to 0.635 cm (0.25 in). A pair of physical stops was added to the end of each

curved support plates to limit the rotation of the gimbal frame in order to protect sensitive components from damage. The final modification was the change of the gimbal shaft bearing from a needle bearing design to a sealed ball bearing design as discussed in the Mechanical Structure Design chapter. These design iterations led to the final gimbal frame prototype that is shown in Figure 36.

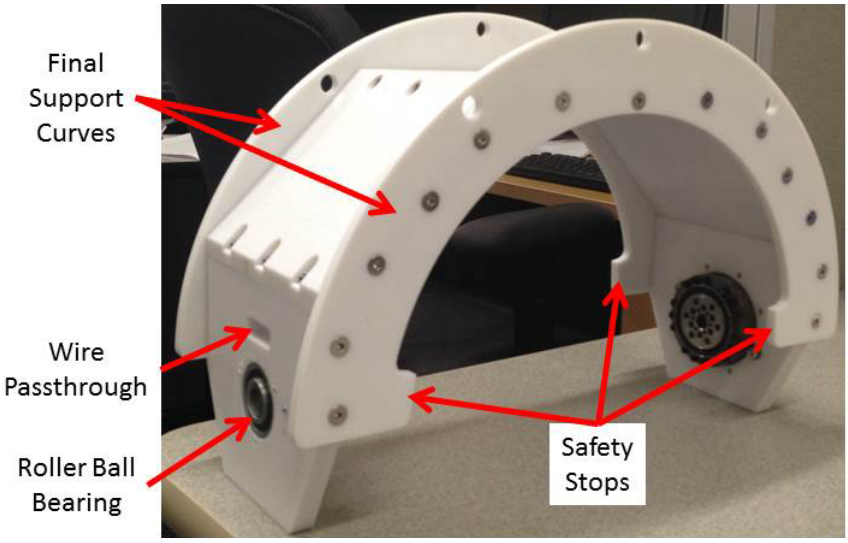

Figure 36. Final gimbal frame prototype (assembled)

Figure 37 shows the partially assembled view of the final gimbal frame prototype with the skew angle set to 90°. This illustrates how the gimbal frame side support plates and the roller rods interact to allow for continuous skew angle adjustment.

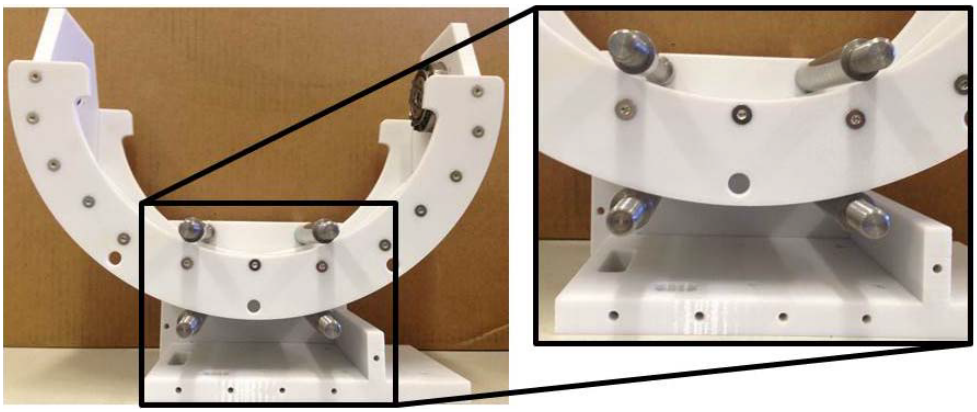

Figure 37. Cutaway of CMG skew angle adjustment mechanism

Figure 38 shows the complete CMG with the Ackman momentum wheel mounted, and positioned at the standard skew angle of 53.4°. Figure 39 shows the system at a skew angle of 90°.

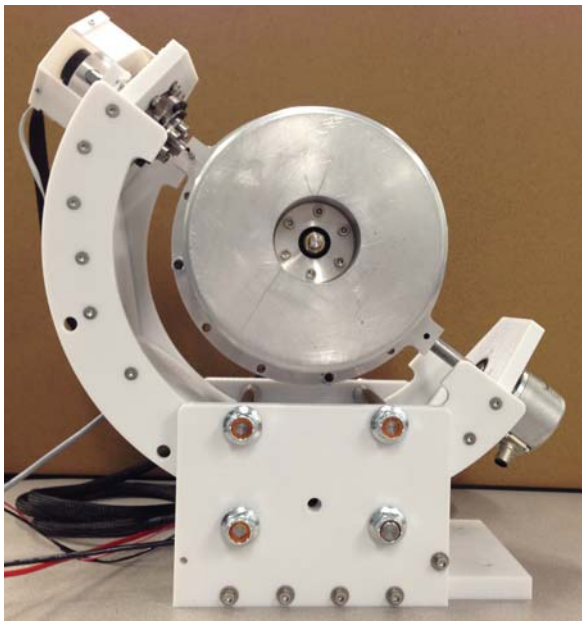

Figure 38. CMG prototype at 53.4° skew angle

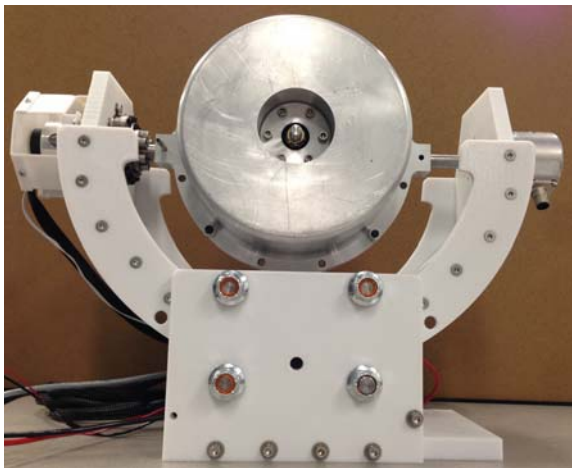

Figure 39. CMG prototype at 90° skew angle

Overall, the use of the 3D printer provided significant time and cost savings during the design and prototyping phase of the project. Without the use of rapid prototyping tools the design would have matured much more slowly as machine shop

time and material procurement times would have driven major delays into producing, fit checking, and function testing of the prototype designs.

C. OTHER 3D PRINTED COMPONENTS

During this thesis the 3D printer was not only used for fit testing and initial functional checkouts, it was also an enabler that facilitated the overall test platform build as it allowed for the quick design and inexpensive production of complex custom components.

1. Battery Holder

In order to incorporate a relatively inexpensive, commercially available rechargeable battery to power the 24 VDC bus it was necessary to create a custom adapter which could allow the battery to be secured to the test platform in order to provide a secure connection to the electrical power connectors.

During very early component functional tests and analysis it was determined that the high power (greater than 10A at 24 VDC) which could be supplied by the chosen battery required that the battery connector have an inline switch to allow for isolation of the positive and negative battery leads to prevent arcing during battery insertion and removal. It was also determined that this battery adapter should be flexible enough to be reused by future systems with little or no modification. In order to meet these two requirements measurements were taken from the physical structure of the DeWalt 24 V XR+ NiCd battery pack.

The DeWalt battery uses a single positive lead and three negative leads for parallel connection of the battery cells to supply the current levels needed to power the contractor grade power tools it was designed for. In designing the battery holder this connectivity was taken into account and a physical barrier was constructed between the positive and negative lead banks to ensure that there was no potential for future short circuits. This also aided in the process of wiring the battery holder for operation since there would be no guess work as to which leads should be ganged together. The single positive lead was selected to be wired to the switch in accordance with typical practice.

The battery measurements were used to develop a CAD design shown in Figure 40, and the battery holder was manufactured using the 3D printer. The fully assembled version of the battery holder is shown in Figure 41. In both figures, the left image shows the top of the battery holder from the direction that the battery installs from in order to show the battery vent opening, the battery connectors, and the switch mounting location. The image on the right is rotated to show the switch mounting location on the right, the separated conduits for the positive and negative battery leads, the banana connector openings designed into the structure, and the battery vent channel.

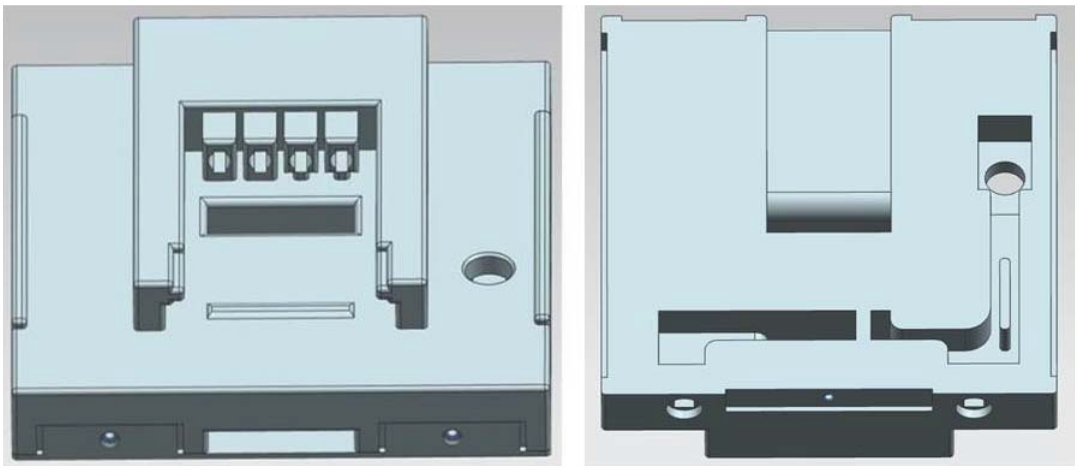

Figure 40. Battery holder CAD model

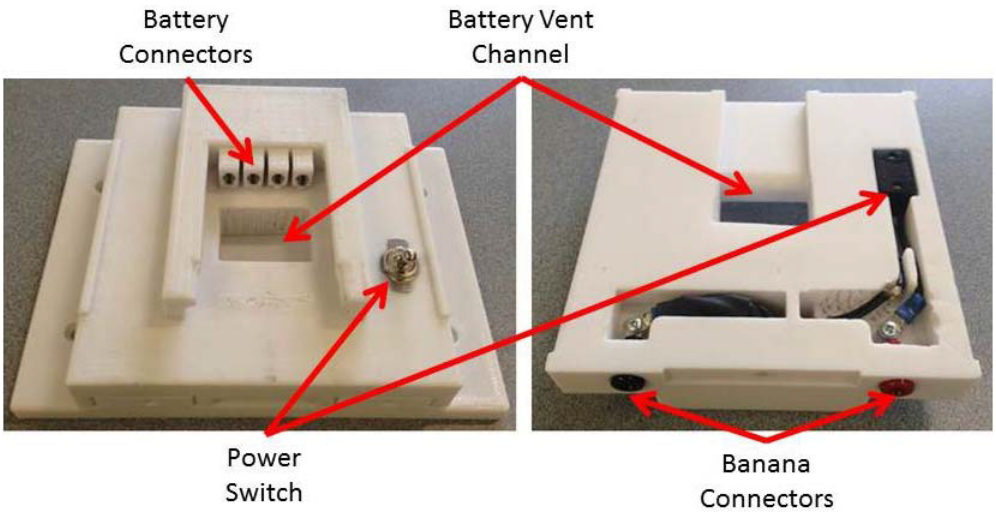

Figure 41. Battery holder fully assembled

The battery vent channel was designed into the battery holder to match up with vents on the contact side of the DEWALT battery. The belief early in the design process was that within the large battery case was housed a small fan which could remove excess heat during battery operation. In practice this battery vent was shown to align with the fan on the battery charger, and is only used during charging operations.

2. Single Degree of Freedom Air Bearing Collar

During the CMG design and build process, work was simultaneously conducted to determine how the system performance could be characterized. The initial plan was to use a new single axis air bearing which was anticipated to be delivered from the vendor during the CMG prototyping phase. Unfortunately, the delivery date for this hardware was later than expected, and a review of other available test apparatus was conducted. During this time it was decided that although a high precision single axis air bearing would be preferred, a 3 degrees-of-freedom (3-DOF) air bearing, with some modifications, could be used for system characterization testing.

A 3-DOF platform is ideal for many satellite simulators that have a full ADCS, which commonly includes three or more reaction wheels or CMGs to control the attitude of the system in all three axes. As the tests to be conducted were to characterize a single CMG, the use of a 3-DOF system would not work. In order to modify the system to only allow 1-DOF, a custom collar was designed which incorporated a group of four sealed roller ball bearings spaced 90° apart. Figure 42 shows the CAD model of the 1-DOF collar on the left and the 3D printed hardware with the bearings installed on the right. This collar allowed for rotation about the yaw (z) axis, while constraining the pitch (x) and roll (y) axes to keep the platform stable.

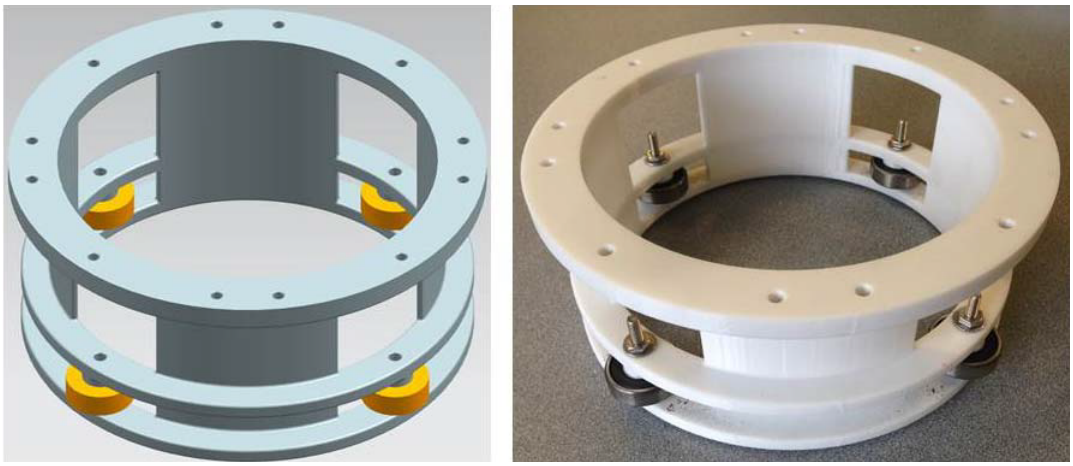

Figure 42. Air bearing 1-DOF collar, CAD model (left), assembled component (right)

Figure 43 shows the 1-DOF collar mounted on the testbed platform with the platform installed on the air bearing pedestal. Figure 44 shows the air bearing platform with the 1-DOF collar installed, and the CMG in test configuration.

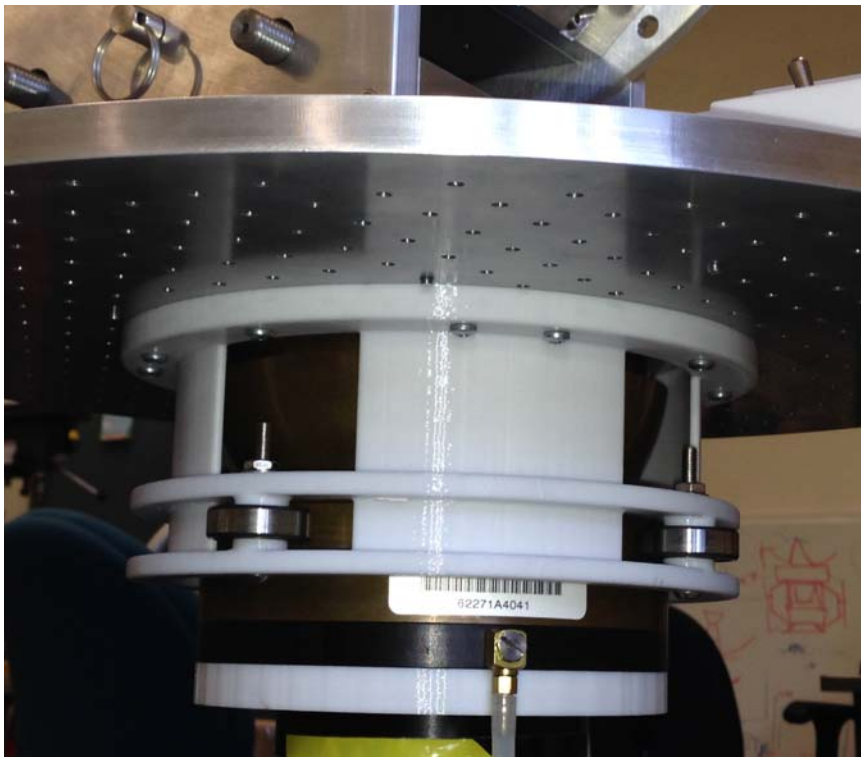

Figure 43. 1-DOF collar installed on air bearing testbed

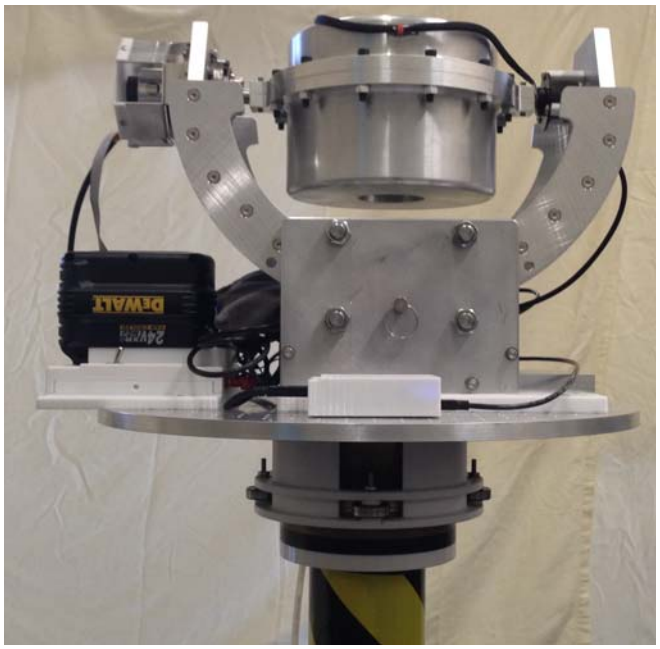

Figure 44. CMG testbed with 1-DOF collar

The complexity and sheer volume of the collar would have been excessively expensive and time consuming to machine from a solid billet of aluminum, whereas the 3D printed version was printed in about a day.

During initial testing it was observed that, although rolling smoothly, the bearings added friction drag which prevented the air bearing from floating freely. The decision was made to adjust the bearings so that they were not in constant contact with the air bearing pedestal. Instead a small gap of approximately 0.159 cm (0.0625 in) between all four bearings and the pedestal, while balanced, was found to reduce the drag sufficiently for testing. Although drag is greatly reduced, the unfortunate side effect is that the test platform rocks slightly back and forth between the two bearings in line with the gimbal axis as the CMG is gimbaled.

3. BBB Case

Another component which needed to be custom designed was a case for the BBB SBC. There were two primary drivers for the need to design a custom case. The first is that the bottom of the board is populated with unprotected electrical connections where the pins are soldered to the bottom of the board. Considering the fact that this computer

was to be mounted on a solid aluminum platform, the risk of shorting out the SBC was very high, and a means to insulate those pins from the platform was required. The second driver was that there needed to be a way to physically attach the SBC to the platform so that it would not slide around during platform rotations.

A number of commercially available BBB cases were evaluated online, but none of them seemed to meet the needs of this system closely enough without the need for modifications. Instead, it was determined that a custom design would be used. The physical dimensions of the BBB connectors (USB, micro-HDMI, Ethernet, etc.), pin clearances and screw hole locations were taken and a relatively simple box was designed which matched the 1.905 cm (0.75 in) bolt hole spacing of the air bearing platform as well as the specific BBB mounting footprint. The bottom side of the case was designed with hexagon shaped cutouts which match the size of a #4 nut. The nuts were included in the design due to the fact that #4–40 screw threads are difficult to cut and are very weak in this polycarbonate material. The top view of the case is shown in the image on the left, and the bottom view of the case is shown in the image on the right in Figure 45.

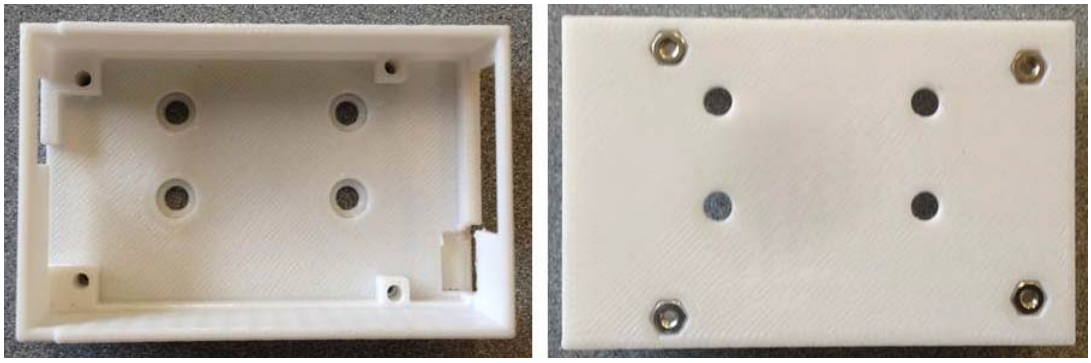

Figure 45. Case for BeagleBone Black single board computer

4. IMU Mounting Plate

The IMU mount was a very simplistic design. As with the BBB case it was necessary to provide a means to attach the IMU to the platform, and to isolate the pins on the bottom side from short circuiting. For this specific installation, a flat plate was designed with a pair of screw hole patterns; one to match the bolt pattern of the platform

and the other to match the screw holes in the IMU board. Additional features of this design are a recessed area corresponding to the location of the soldered pins on the IMU board which allows the IMU to be flat mounted to the plate, and like the BBB case hexagon shapes matching the outer dimensions of #6 nuts were designed into the underside of the plate to facilitate the flat mount of the plate to the platform. These design features are depicted in Figure 46 with the top side view on the left and the bottom view on the right.

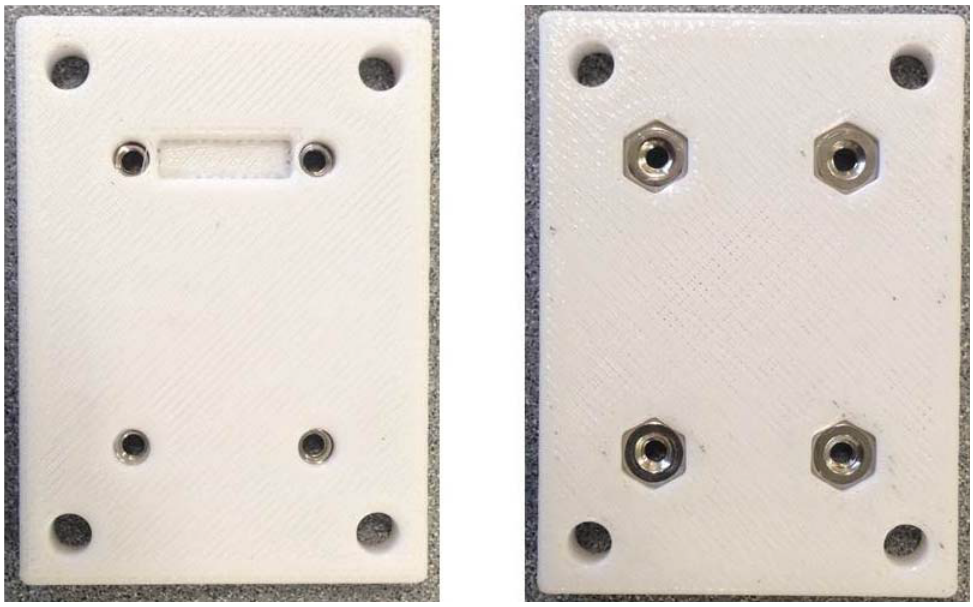

Figure 46. IMU mounting plate

5. CMG Base to Air Bearing Platform Adapter Plate

Another custom design for this system is an adapter plate for mounting the CMG base to the air bearing platform, shown in Figure 47. The CMG mount base is designed with threaded ¼-20 screw holes which are spaced to match the pre-existing bolt pattern used to attach the CMG to the R-SAT platform. Due to the fact that the screws pass through from the top of the R-SAT deck to engage with the threads in the mount base, and that the test configuration for the CMG on the 1-DOF air bearing is "upside down," it is necessary to install the bolts from the bottom side of the adapter plate into the CMG mount base. This accounts for one set of screw attachments. The second is through a

series of eight slotted #8 screw holes from the top of the adapter plate into the 1-DOF platform. These slotted holes were designed with a counterbore to minimize the protrusion of the bolt heads above the plate, and are used for making coarse testbed balance adjustments when installing the CMG components on the platform. Figure 47 shows the CAD model of the adapter plate.

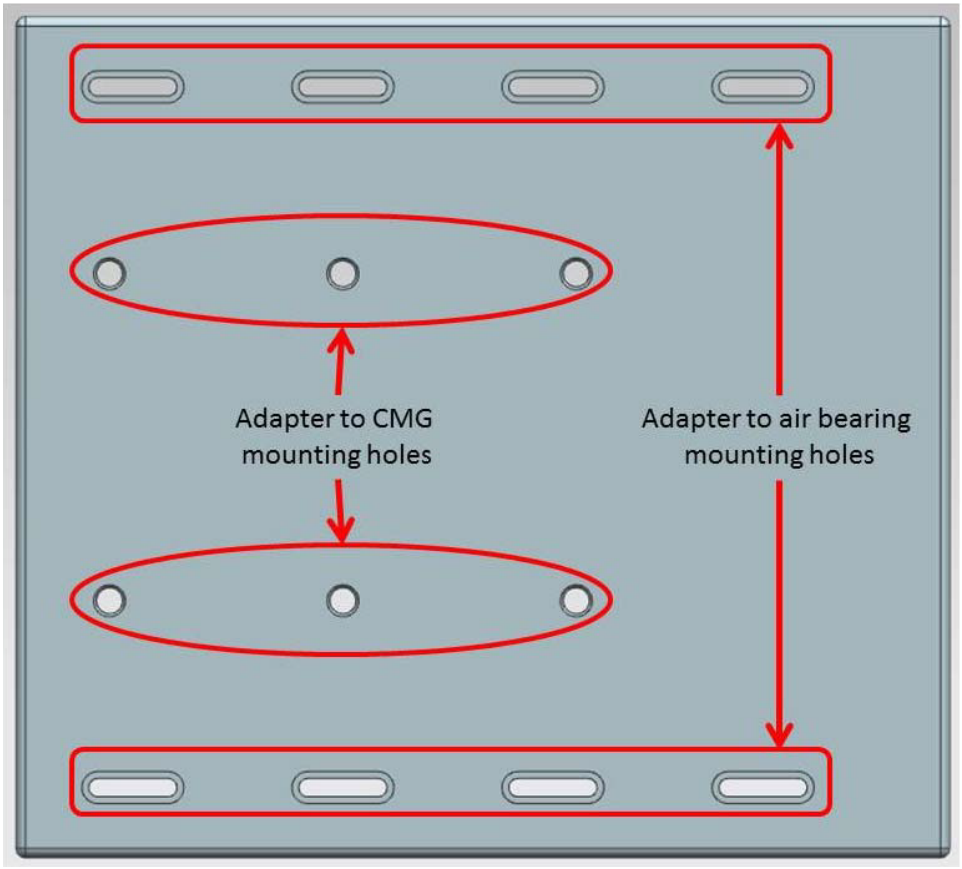

Figure 47. CMG to 1-DOF platform adapter

Unlike the other components discussed so far, this plate was 3D printed using the sparse printing mode. Sparse printing allows for larger objects to be constructed with an internal mesh structure rather than from solid material. In this specific application, the large size of the plate (22.86 cm x 25.4 cm x 1.27 cm) would have an used excessive amount of material (737.4 cm^3 of polycarbonate and 16.4 cm^3 of BASS). Instead, the sparse printed version of the plate only required 295 cm^3 of polycarbonate material and 16.4 cm^3 of BASS. This reduction in material is important when material costs are

considered. The polycarbonate and BASS materials cost approximate $4.50 per 16.4 cm^3 (1 in^3), so the sparse printing saved about $100 in material costs. Moreover, the printer required only half as much time to print the sparse object compared to a solid print of the same part. If this part had been solid printed, it would have actually been cheaper to machine it from an aluminum plate even after paying for machine shop labor.

D. SUMMARY

As this chapter has demonstrated, the value of the 3D printer to the completion of this thesis cannot be overstated. The rapid prototyping of the CMG frame components allowed for fit checking and functional testing without the need to procure excess raw materials, or to wait in the machine shop queue for production of components that could require redesign after initial testing. The strength of the polycarbonate material was also found to be sufficient to mount the actual Ackman momentum wheel and all of the gimbal components in the prototype frame and conduct initial functional testing with the momentum wheel spinning at full speed and rotating the CMG about its gimbal axis.

Additionally, the 3D printer was used to fabricate custom end-item components which were used in the CMG testbed. It is actually in this area that the 3D printer provided the greatest benefit to the project, and allowed for rapid design and fabrication of vital components. Some of these components, like the 1-DOF collar, would have been exceedingly expensive and complex to machine from a billet of solid aluminum, whereas the 3D printer was able reduce manufacturing time as well as material cost.

V. SYSTEM CHARACTERIZATION

A. INTRODUCTION

This project was conducted as a two part effort. The first part was the design and fabrication of the CMG and the necessary test apparatus as has been discussed in the previous chapters. The second part of the project was to use the integrated CMG and testbed to assess and characterize the performance of the CMG design. This chapter will discuss the series of tests that were conducted and their results.

B. TESTBED CONFIGURATION

The first aspect to discuss is the unique test configuration that was used to characterize the performance of the CMG. Many of the components of the testbed have been discussed in the previous chapters, but it is necessary to discuss how those components were combined to enable the characterization tests and some of the limitations of the setup. A photo of the initial test configuration is shown in Figure 48.

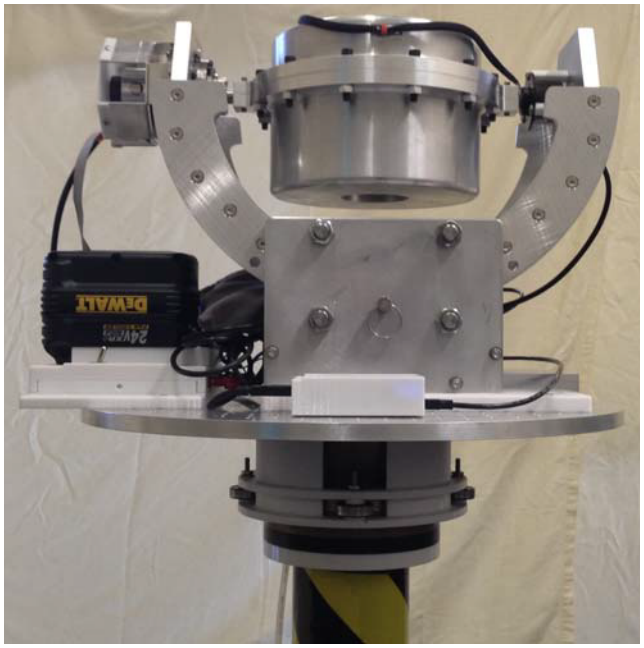

Figure 48. Initial CMG test configuration

1. 1-DOF Air Bearing Collar

As discussed in the Rapid Prototyping chapter, a 1-DOF air bearing testbed was developed by modifying an existing 3-DOF air bearing with a custom collar that was manufactured to constrain the pitch (x) and roll (y) axes of the testbed allowing only rotation about the yaw (z) axis. The collar worked well at preventing the platform from tipping over, but the four sealed roller ball bearings introduced friction, which is not present in 3-DOF simulators. During initial functional testing, it was determined that this friction was too high for use in a spacecraft simulator. The total amount of friction was reduced by attempting to balance the platform and by adjusting the bearings outward so that all four were not simultaneously in contact with the air bearing pedestal.

Spacing the bearings greatly reduced the total amount of friction in the system as compared to operation with all four bearings in contact. Unfortunately, a side effect of the gaps is that as the CMG gimbaled, the center of mass of the platform shifted slightly causing the platform to rock back and forth between the two bearings which were aligned with the gimbal axis of the CMG. This rocking caused small disturbances in the IMU measurements, but overall had no significant effect on system characterization. In order to characterize the impact of the bearing rolling resistance the rate of platform deceleration due to the bearing friction was calculated from test data. In order to keep the platform as stable as possible for this test, the momentum wheel was used to impart the torque on the platform which caused the rotation. The momentum wheel was used much like a reaction wheel is used in other spacecraft systems. The gimbal angle (δ) of the momentum wheel was set at 180°, the CMG skew angle was locked at 90°, and the momentum wheel was spun up to 5000 rpm. The momentum wheel speed was then commanded to 0 rpm using a 100 rpm/s ramp rate. This spin down transferred all of the rotational momentum of the wheel into the testbed platform. The maximum platform rotation rate was measured, and the rate of platform deceleration was measured and calculated once the wheel came to rest.

Multiple attempts were made to use the rate and acceleration data directly from the IMU, but calibration of the gyro and accelerometer could not be completed successfully. Therefore, during the long duration of this test, the gyro drift became

unmanageable. Instead of using the IMU data, an estimate of the deceleration was obtained by calculating the period of platform rotation from the platform position data. Although the actual position output by the IMU's magnetometer was unlikely to be accurate, the period of the platform revolutions was validated using a stopwatch. The test shown in Figure 49 was chosen for this system characterization. The blue data points are the position output from the IMU, and the red dots at or near the zero crossovers were used as the data points from which the rotational period was calculated. Calculating the time for each of the 21 platform revolutions over this 368 second timeframe provided a deceleration rate of approximately 0.075 °/s^2 over the range of platform rates between 30 °/s and 10 °/s. Although this rolling resistance was present in the system, the effect was minimal for the characterization tests which were run. The rate of platform rotation calculated as the average over an entire rotation period, and the associated platform deceleration is plotted in Figure 50.

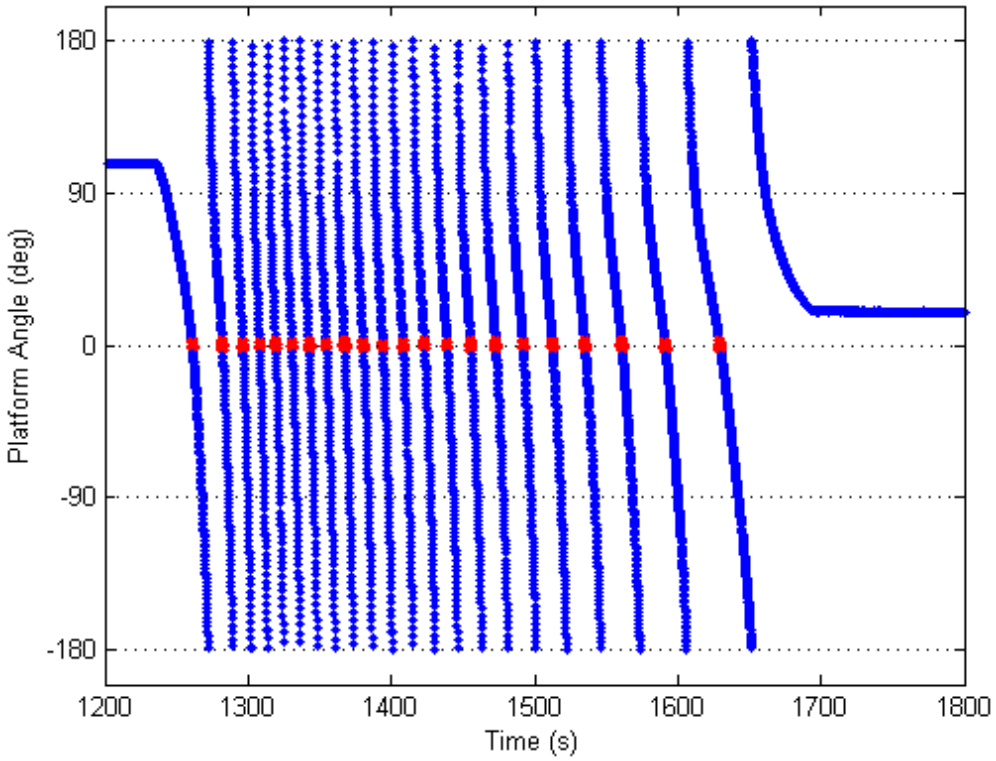

Figure 49. Platform rotation period during deceleration

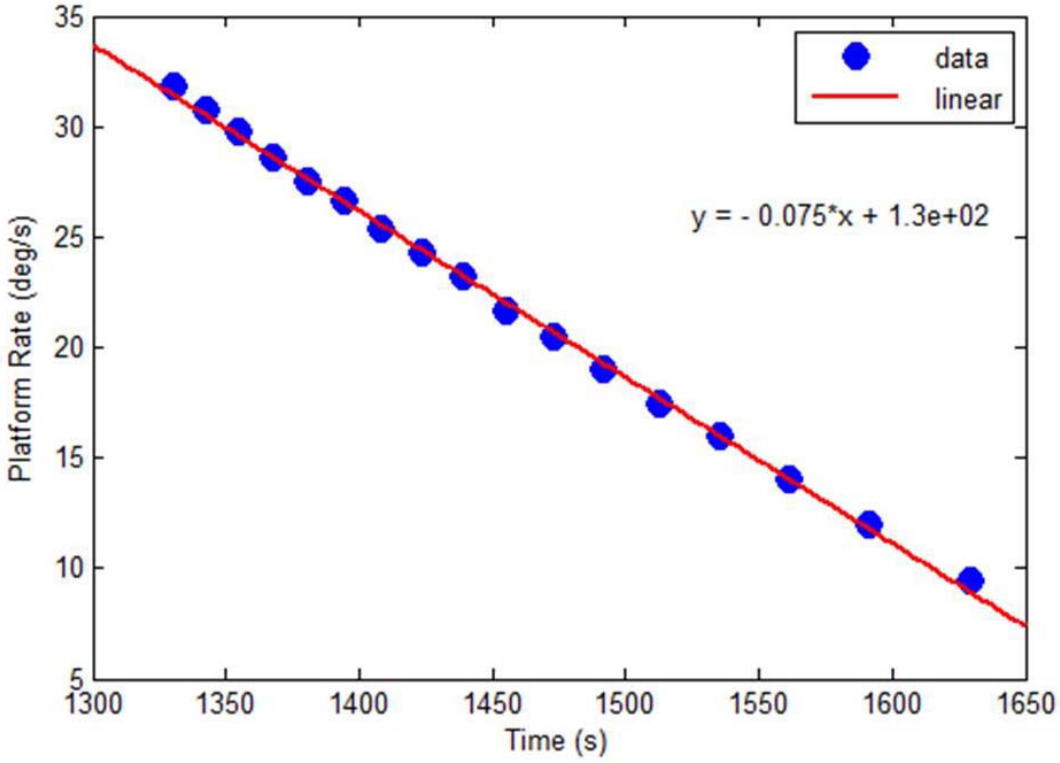

Figure 50. Platform rotation rate and deceleration rate

Using Equation (9) with α = 0.075 °/s^2 and the estimated testbed moment of inertia I_Z the amount of CMG output torque that is lost due to this friction can be approximated. Assuming that I_Z = 10.57 kg-m^2 (computation shown later in this chapter) the friction torque is estimated at 0.014 Nm.

$$\tau = I_z \alpha \tag{9}$$

2. Testbed Center of Mass

One additional testbed issue to mention is the platform center of mass. In a well-balanced 3-DOF testbed the center of mass of the platform is coincident with the platform rotation point, which is at the center of the brass ball that is supported by the cushion of air from the air bearing pedestal. For this test configuration, the center of mass was several centimeters above the center of rotation. The instability caused by having the center of mass above the rotation point was also a significant driver in the need for the 1-DOF collar. If further effort were put into lowering the center of mass of the platform, the

improved balance would further reduce the force applied to the bearings as they come in contact with the pedestal, and bearing drag effect could be reduced.

C. CMG OUTPUT TORQUE TEST

The primary reason for calculating the testbed rolling resistance was to better characterize the CMG output torque by monitoring the platform acceleration measured by the IMU during gimballing operations. Unfortunately, the IMU did not provide reliable rotation rate or acceleration values which could be used for this output torque test. For this reason the CMG output torque is 0.136 Nm/°/s as calculated in Table 3, but could not be validated through testing during this project. It is recommended that a different IMU be installed on the testbed in order to correct the issue and enable the output torque test to be performed.

D. MOMENTUM WHEEL RATE TEST

The first test to be discussed is the initial characterization of the performance of the Ackman momentum wheel. In this test, the wheel was spun up to a steady state speed of 5000 rpm and the current draw at this rate was determined from the data set. The results of this test, shown in Figure 51, illustrate the momentum wheel motor power usage relative to its 50W rated power. In this image the stacked plots on the left show the performance of the motor when it is spinning at 5000 rpm in the clockwise (CW) direction, and the plots on the right show the performance when the motor is spinning at 5000 rpm in the counterclockwise (CCW) direction. The CW and CCW directions are defined from the motor case side of the momentum wheel as shown in Figure 52. The test was conducted in both directions in order to determine if there was any appreciable difference, and to establish a baseline for operation in either direction.

In both the CW and CCW plots the wheel speed is held at a constant 5000 rpm. CW wheel operation draws an average of 43W, while CCW operation draws an average of 39W. This difference in power consumption was seen consistently through the other tests which will be presented. In all cases the CCW power consumption is lower than the CW consumption. The root cause of this effect was not identified during this project, but

it is hypothesized to be an effect of the preload on the duplex bearing in the momentum wheel.

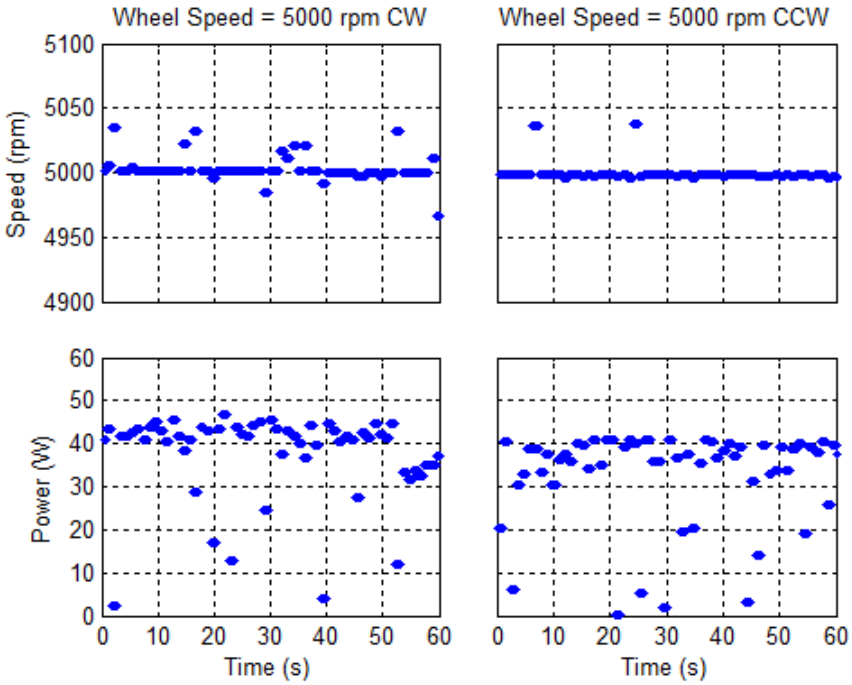

Figure 51. Momentum wheel power consumption at 5000 rpm, CW rotation (left) CCW rotation (right)

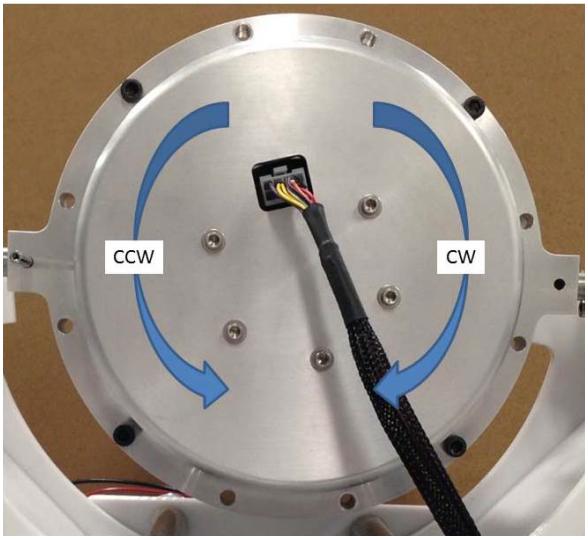

Figure 52. Momentum wheel motor spin direction, motor side case view

The primary takeaway from this test is that the Maxon EC45 motor provides sufficient power to spin the momentum wheel at the desired maximum speed of 5000 rpm. If the motor were unable to achieve the 5000 rpm, or were struggling to maintain the speed, the power levels would be nearly at the 50W maximum available, which was not the case. The reserve available power, the difference between the rated and nominal power levels, is an important margin for maintaining momentum wheel speed while transferring momentum through gimballing. If there were not enough motor power available to overcome the motor deceleration caused by the effects of gimballing, the wheel would lose excessive speed which could adversely impact the spacecraft attitude control system.

E. GIMBAL RATE VS GIMBAL MOTOR POWER CONSUMPTION

The purpose of this test was to verify that the gimbal motor was capable of providing at least the industry standard 1 rad/s gimbal rates with the momentum wheel spinning at its full operational speed of 5000 rpm. The early attempts at conducting this test were unsuccessful due to excessive CMG back drive resulting from rapid rotation of the testbed platform. The low moment of inertia (MOI) of the original setup allowed the platform to rotate at relatively high rates exceeding 10 rpm during gimbal operations, with a maximum observed rate of over 100 rpm during a full momentum wheel stop operation. Not only are these rates not representative of normal spacecraft operation, but the torque coupled into the CMG from the platform rotation exceeded the maximum power of the gimbal motor, even with the 100:1 gear ratio of the harmonic drive. This back drive effect was documented in [4], and was clearly observed in this test. Two separate issues were identified for further characterization from this test failure.

The first was to calculate the MOI of the platform and adjust the MOI in order to allow for full operation of the CMG. The MOI was increased though a series of incremental additions of mass and moment arms. The final testbed configuration consisted of the 36.14 kg test platform and the addition of two 1.702 m aluminum channels mounted to the platform at their midpoints and a 3 kg mass installed at each of the four extreme channel ends, as shown in Figure 53. The midpoint mounting of the

aluminum moment arms provided a balanced arm which applied minimal load on the mounting screws for moment arms of 0.8956 m from the center of the platform.

In order to quantify the MOI of the test bed about the rotation axis the fully constructed platform, without the arms installed, was weighed and the platform was modeled as a solid disk with equally distributed mass. Using Equation (10), with a platform mass of m = 36.14 kg and a radius of r = 0.2286 m gave I_Z = 0.944 kg-m^2. Although this method may be slightly inaccurate, it provides a simple way to estimate the MOI.

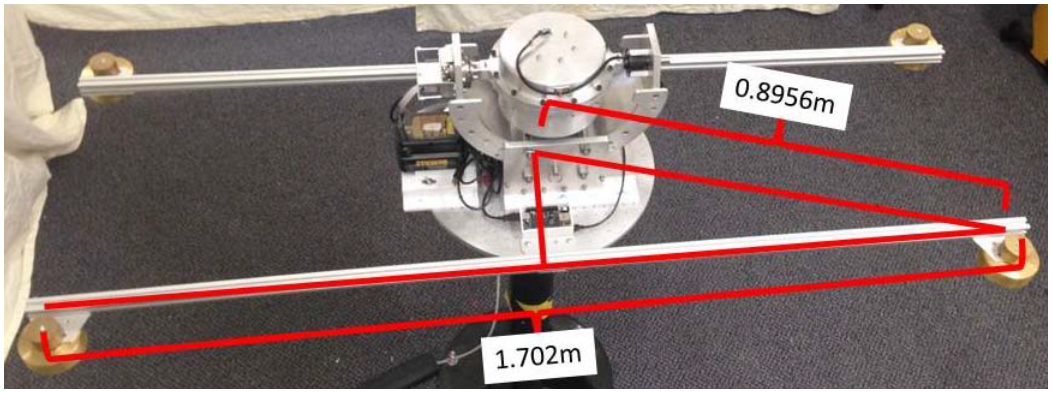

Figure 53. Testbed with moment arms installed

$$I_z = \frac{mr^2}{2} \tag{10}$$

With the MOI of the platform about the rotation axis calculated, it is now possible to calculate the change in MOI of the final configuration with the moment arms attached using Equation (11). Using m = 3 kg masses for each of the four masses mounted a distance r = 0.8956 m from the platform center, the change in MOI was 9.625 kg-m^2. The final MOI for the platform was calculated by adding Equations (10) and (11). The new setup has a MOI of 10.57 kg-m^2, more than a full order of magnitude greater than that of the initial testbed setup.

$$\Delta I_z = 4mr^2 \tag{11}$$

The gimbal rate test was conducted on the modified testbed with the momentum wheel spinning at a constant rate of 5000 rpm. The gimbal motor was issued a 1 rad/s step command that held as the momentum wheel was gimbaled through 5 full rotations. The resulting gimbal rate, gimbal motor power consumption, and gimbal position are plotted in Figure 54. The stacked plots on the left illustrate the gimbal motor rotation in the CW direction, and the plots on the right show the rotation in the CCW direction. Gimbal position angles of 0° and 180° are the angles in which the momentum wheel rotation axis is vertical and angles of -90° and 90° correspond to a horizontal momentum wheel rotation of axis. The constant 1 rad/s slope shown in the gimbal position plots illustrates that the gimbal motor is fully capable of meeting its 1 rad/s gimbal requirement with the momentum wheel running at normal speed, and on a spacecraft with a MOI that is sufficient to prevent excessive CMG back drive. Figure 55 shows a close up view of a single gimbal rotation from the data set plotted in Figure 54. The single gimbal rotation plot provides a better view of a cyclic gimbal motor power fluctuation that is present during all gimbal tests.

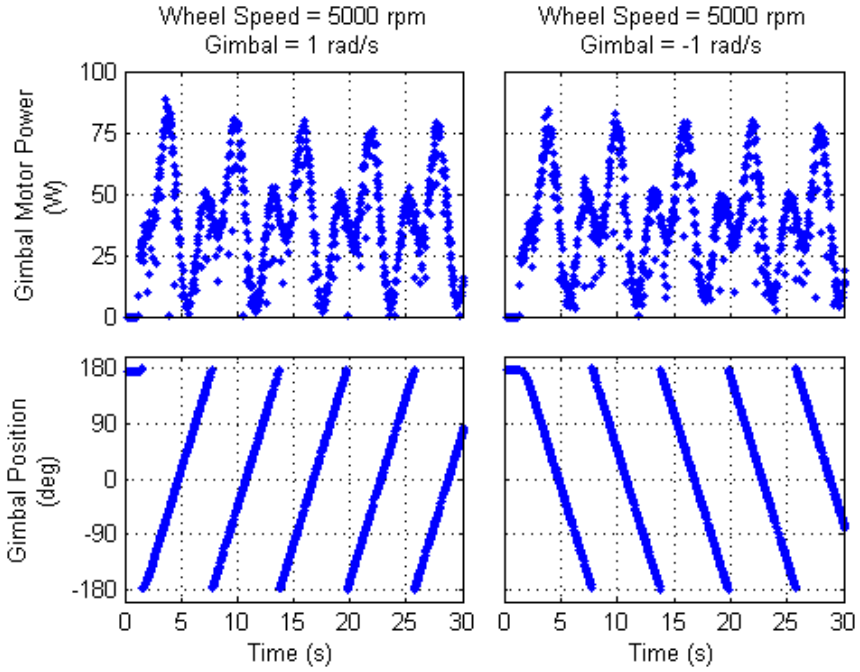

Figure 54. Gimbal motor power consumption at 1 rad/s gimbal rate, testbed floating

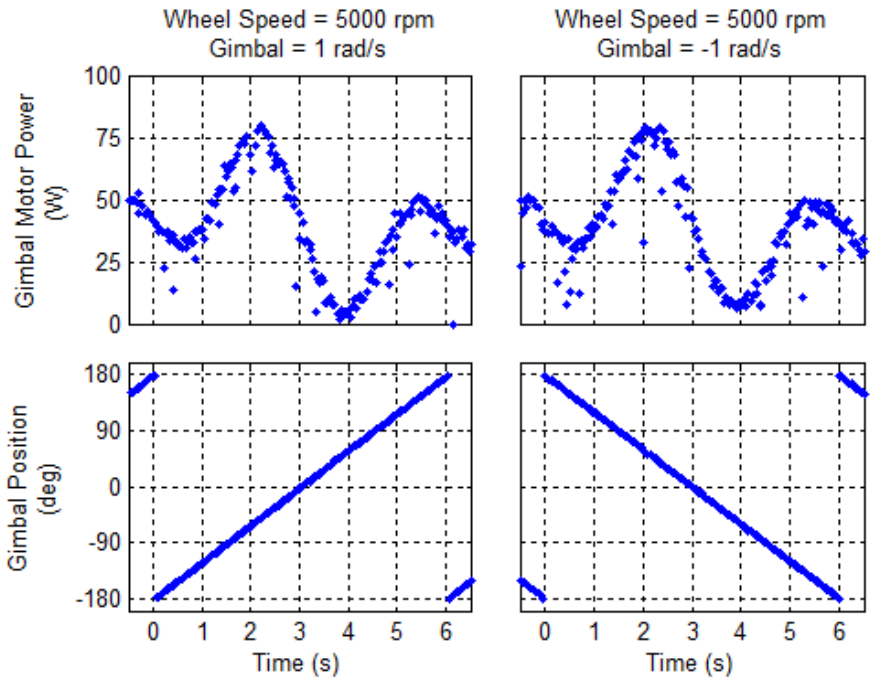

Figure 55. Gimbal motor power at 1 rad/s gimbal rate, single gimbal revolution

The second issue to be characterized was the magnitude of the back drive torque caused by the rotation rate of the platform. In order to remove the back drive effects from influencing the operation of the CMG gimbal motor, a test was conducted with the same inputs to the momentum wheel and gimbal motors (5000 rpm and 1 rad/s, respectively), but the platform was constrained so that it could not rotate. A single, representative gimbal revolution from this test is plotted in Figure 56.

The gimbal power consumption plots illustrate a gimbal motor loading issue that is specific to the design of this momentum wheel. Normally a constant power draw would be observed. However, the current design of the momentum wheel is such that the gimbal axis is unbalanced. There is more mass on one side of the gimbal axis than on the other. This unbalance would be less significant in a space based system subject to microgravity, but in a terrestrial testbed the work done by the gimbal motor varies as the unbalanced mass rotates. This phenomenon is manifest as the cyclic power oscillations in the plots. This unbalance also further exacerbated the back drive effects (see Figure 55) as the gimbal motor needed to draw power at levels above the continuous power rating of 50 W. Since the transients are below the current limited (5A) instantaneous power limit

(120W) of the motor controller the gimbal can overcome the back drive effect. Figure 55 illustrates a single gimbal revolution for closer inspection of the gimbal angles at which the motor draws its peak power requirements.

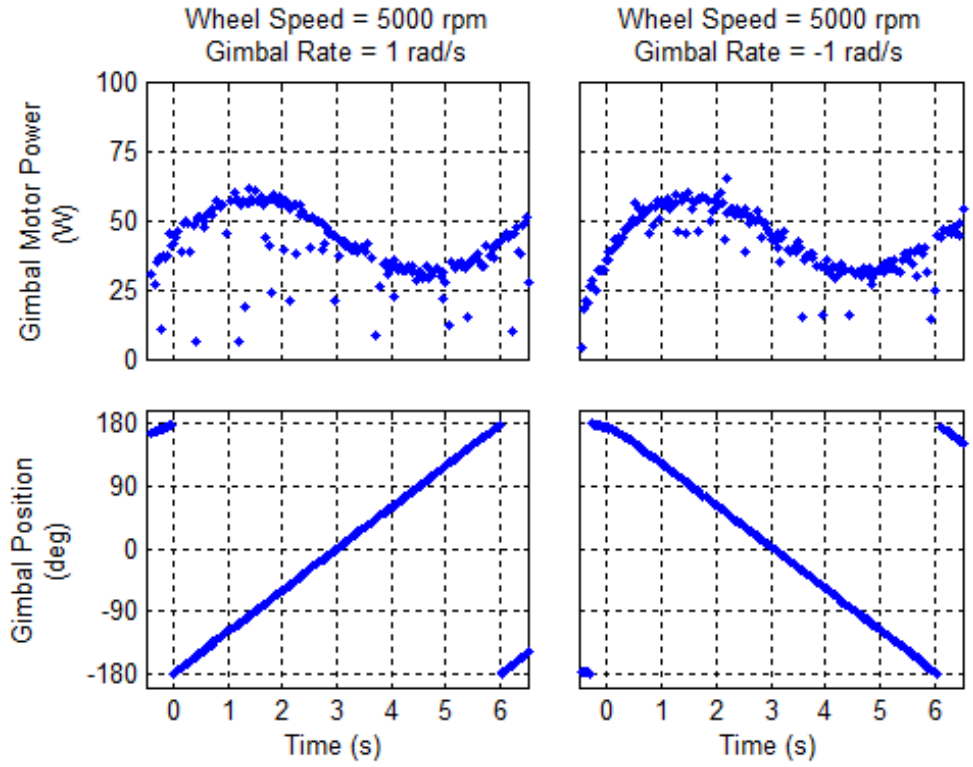

Figure 56. Gimbal motor power at 1 rad/s gimbal rate, testbed rate = 0 rpm

In order to further evaluate the gravity effects on the gimbal motor a test was run with the momentum wheel rotor stopped so that the gimbal motor did not have to overcome the influence of the momentum stored in the wheel. The results of these three tests are plotted together in Figure 57.

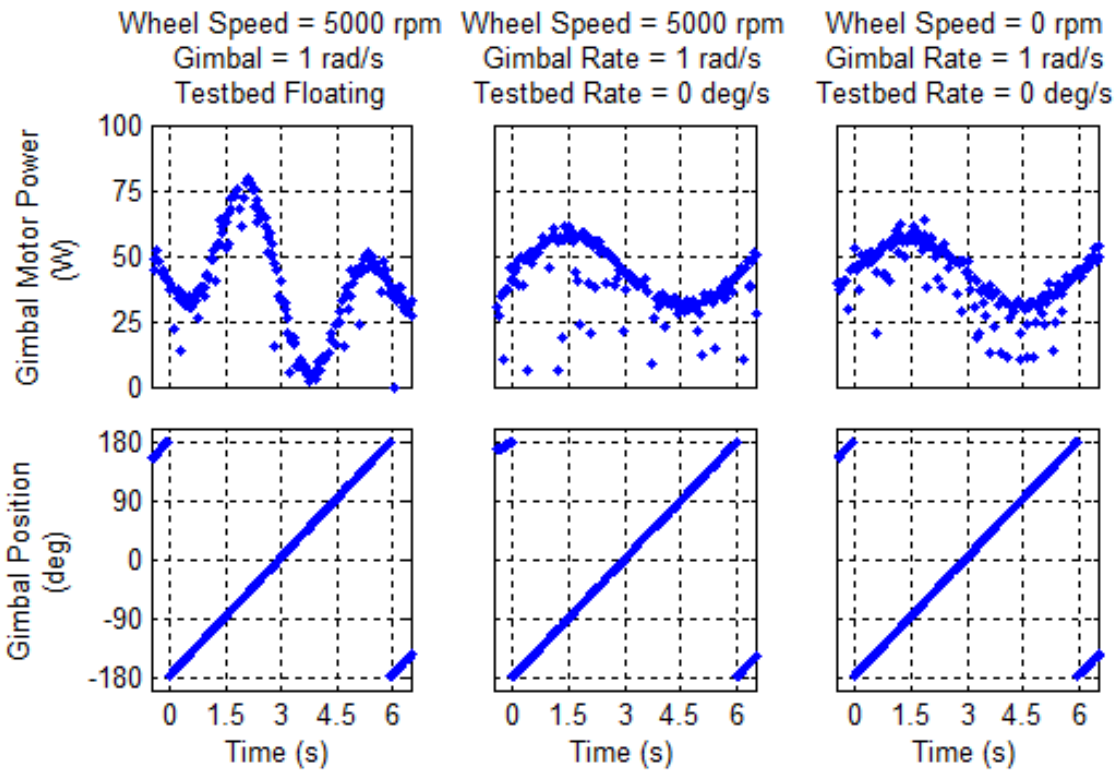

Figure 57. Combined gimbal motor power consumption plots.

The test results plotted in Figure 57 illustrate two interesting results. The first is seen when comparing the middle column of plots to the right column of plots. A comparison of the gimbal motor power consumption plots with the platform fixed shows a negligible effect of the stored wheel momentum on the gimbal motor power draw. The plots also show that the power peaks, both above and below the average power draw of 41.2 W, align with the gimbal angles corresponding with the horizontal momentum wheel rotation axis. It is at these angles that the maximum gravity torque (τ_g) is applied to the motor, as shown in Equation (12). In Equation (12), r_m is the distance from the gimbal axis to the center of mass of the momentum wheel assembly, m is the mass value at that point, and the sine (vice cosine due to the definition of the δ axis) of the δ angle is used to scale the effect of gravity as the mass imbalance rotates.

$$\tau_g = r_m m g \sin\delta \tag{12}$$

The value of τ_g can be used to calculate the unbalance of the momentum wheel using Equation (13) where N_g is the gear ratio of the harmonic drive, K_t is the torque constant of the gimbal motor, and i is the motor current at angle δ. By setting Equations (12) and (13) equal to each other and solving for the combined mass and radius ($r_m m$) the unbalance can be calculated, and the amount of mass which would need to be added to the opposite side of the momentum wheel case can be determined. For N_g = 100, K_t = 33.5 mNm/A and max i = 2.46 A, g = 9.807 m/s^2, and δ = 90°, $r_m m$ is calculated to be 0.0094 kg-m. Therefore, at a distance of r_m = 0.048 m (the center of a mass which would be added to the outside of the motor case), a mass of m = 2.06 kg should balance the wheel about the gimbal axis.

$$\tau_g = N_g K_t i \tag{13}$$

$$r_m m = \frac{N_g K_t i}{g \sin \delta} \tag{14}$$

The second result that can be seen in Figure 57 is the difference in gimbal motor power consumption between the left column plots and the other two columns. The peak-to-peak value of gimbal motor power in the left plot is 76 W, and the corresponding values for the middle and right plots is only 27 W. While the 27 W difference is due to the gravity effects on the unbalanced momentum wheel, the 76 W difference is the combined effects of gravity plus the power necessary to overcome the CMG back drive torque. The back drive torque applied to the gimbal shaft can be calculated using Equation (15), which is expanded into Equation (16). By defining τ_b as the gimbal shaft torque at the output of the harmonic drive the gimbal motor torque can be used to estimate the platform rate by setting Equations (15) and (17) equal to each other which leads to Equation (18).

$$\tau_b = \omega_{platform} \times h_{wheel} \tag{15}$$

$$\tau_b = \begin{bmatrix} 0 \\ 0 \\ \omega \end{bmatrix} \times \begin{bmatrix} 0 \\ h\cos\delta \\ h\sin\delta \end{bmatrix} = \begin{bmatrix} -\omega h\cos\delta \\ 0 \\ 0 \end{bmatrix}^{cmg} = \begin{bmatrix} -\omega h\sin\delta \\ 0 \\ 0 \end{bmatrix}^{platform} \tag{16}$$

$$\tau_b = N_g K_t \Delta i \tag{17}$$

$$\omega = \frac{-N_g K_t \Delta i}{h\sin\delta} \tag{18}$$

Note that in Equation (18), ω = ∞ when δ =+/- π, which implies that the back drive effect is null for center configurations of the CMG, i.e., when the vectors *h* and ω are aligned. On the other hand, when δ =+/- π/2, the value of ω is the smallest, therefore the back drive effect is a maximum.

The first calculation that was performed using Equation (18) was to determine the maximum platform rate at which the gimbal motor output torque, at the maximum 120 W level, could sustain a 1 rad/s gimbal rate. The result of this calculation is that for platform rates up to 65.0 °/s full gimbal control can be maintained for short periods of time (less than 5 seconds before the safe mode of the controller is activated).

This value cited above was calculated for a constant platform rate, but in observing the results plotted in Figure 55 the peaks in the floating platform plots are seen to occur at gimbal angles of approximately -60° and 60 degrees. The power consumption peaks for the fixed platform tests correspond to the orientation of the greatest gravity torque resulting from the mass difference, which occurs at gimbal angles of -90° and 90°. As such, the maximum back drive torque was expected to occur at these same angles. The shift in the gimbal angle at which the peak back drive torque occurs in this test is due to the fact that for this specific maneuver the platform had an initial 0°/s rotation rate and δ = 180°. Due to conservation of momentum, and the fact that the CMG was applying a torque to the platform as it was gimbaled, the maximum rotation rate of the platform would correspond with δ = 0°. The increased rotation rate dominates the *sin(δ)* term (assumed constant in Equation (18)), and the peak back drive torque combined with the

gravity torque on the unbalanced momentum wheel case shifted the peaks to -60° and 60°.

In order to characterize the wheel performance if the gimbal axis was balanced, a series of five additional gimbal tests were run with a momentum wheel speed of 0 rpm, a testbed rate of 0°/s, and gimbal rates of 1.0, 0.75, 0.5, 0.25, and 0.1 rad/s. The results of these tests are shown in Figure 58 with the mean value plotted for each case. This mean value is the estimated power consumption if the wheel is balanced. From these plots the increase in gimbal rotation resistance can be seen as the gimbal rate increases. This is related to the friction effects of the drive train.

Using the mean power consumption of 43 W for δ = 1 rad/s from Figure 58, leaves about 7 W available for rejecting the back drive torque. Applying Equation (18) gives a maximum platform rotation rate of 7.2 °/s without exceeding the nominal 50 W rated power of the gimbal drive.

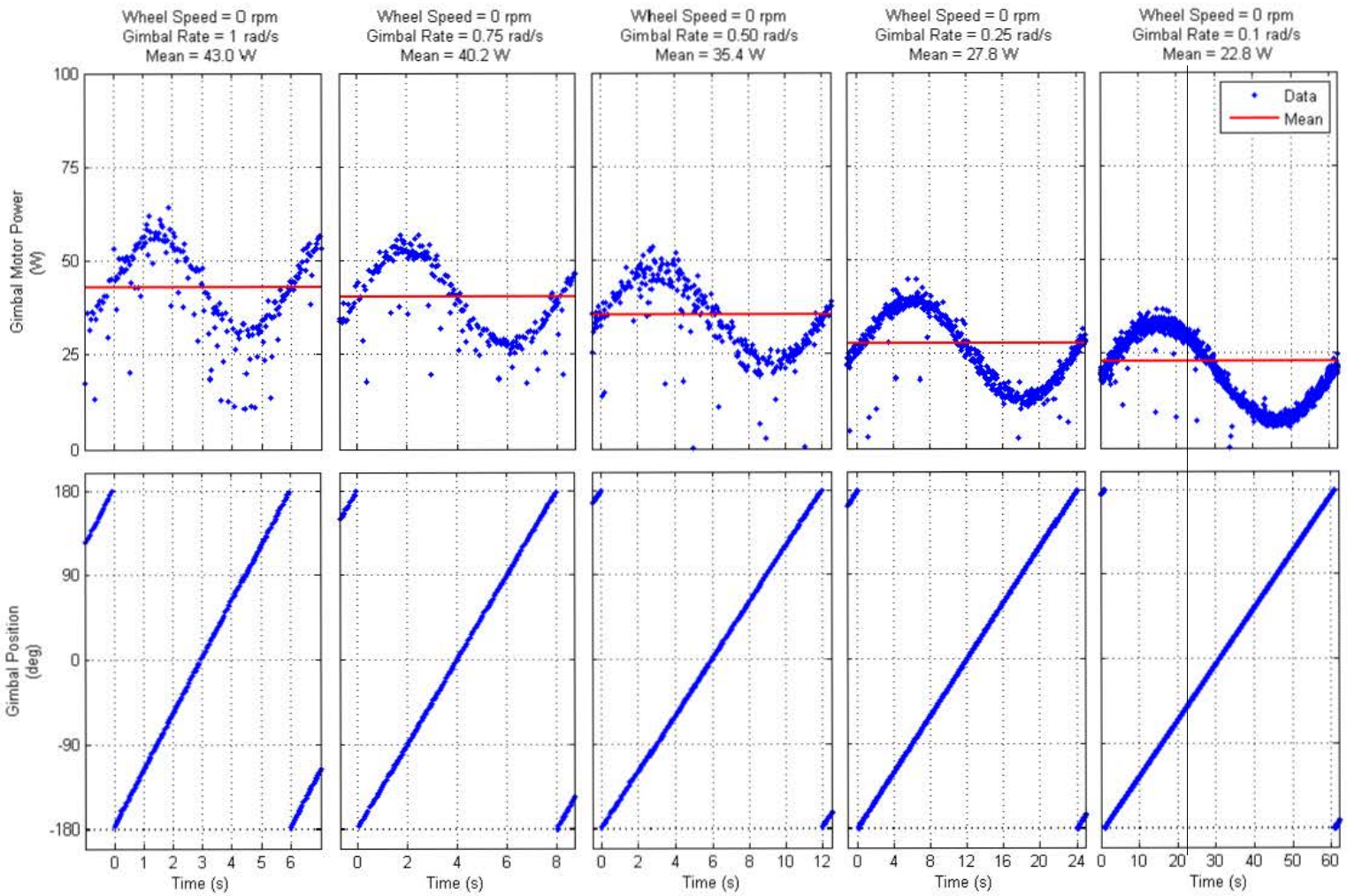

Figure 58. Gimbal motor power consumption

F. MOMENTUM WHEEL SPEED CONTROL

Another important aspect of the operation of a CMG is related to how well the momentum wheel can maintain its speed while it is gimbaled. It is through the gimballing of the momentum wheel that the momentum from the wheel is transferred to the platform in the form of an integrated output torque. The actual momentum stored in the wheel is directly proportional to the rate at which the wheel is spinning, and if the wheel loses speed it also loses momentum thus reducing the output torque of the CMG. This loss of available torque is not just inconvenient it also presents a significant problem for the CMG control law. The control law is designed with an expected CMG torque. In a closed loop control system this loss of torque can be compensated for to an extent, but the maneuver will be off-nominal due to the necessary corrective action of the control.

In order to characterize the amount of speed that the momentum wheel loses during gimballing, a series of eight tests were conducted using different gimbal rates of 0.25 rad/s (Figure 59), 0.5 rad/s (Figure 60), 0.75 rad/s (Figure 61), and 1.0 rad/s (Figure 62) in both the positive and negative gimbal directions. The results shown in these figures are from the tests run with momentum wheel spinning in the CW direction. The same tests were run with the wheel spinning in the CCW direction with no discernable differences in system response. The plots are therefore omitted. These tests were conducted to characterize a total accumulated loss of wheel speed in an extreme scenario where a constant gimbal rate was applied for approximately 1 minute. The higher gimbal rates (0.5 rad/s and greater) are primarily used for slewing the spacecraft, and these inputs are applied over short periods during the “bang” phase in a “bang-coast-bang” maneuver, with low gimbal rates used for fine control during the “coast” phase, or for satellite pointing.

In the slower gimbal rate tests at 0.25 rad/s and 0.5 rad/s there is very little drop in wheel speed with the only noticeable drop being seen at the very end of the -0.5 rad/s case. The speed only dipped to about 4975 rpm from the steady state speed of 5000 rpm, a loss of approximately 0.5% of the wheel speed.

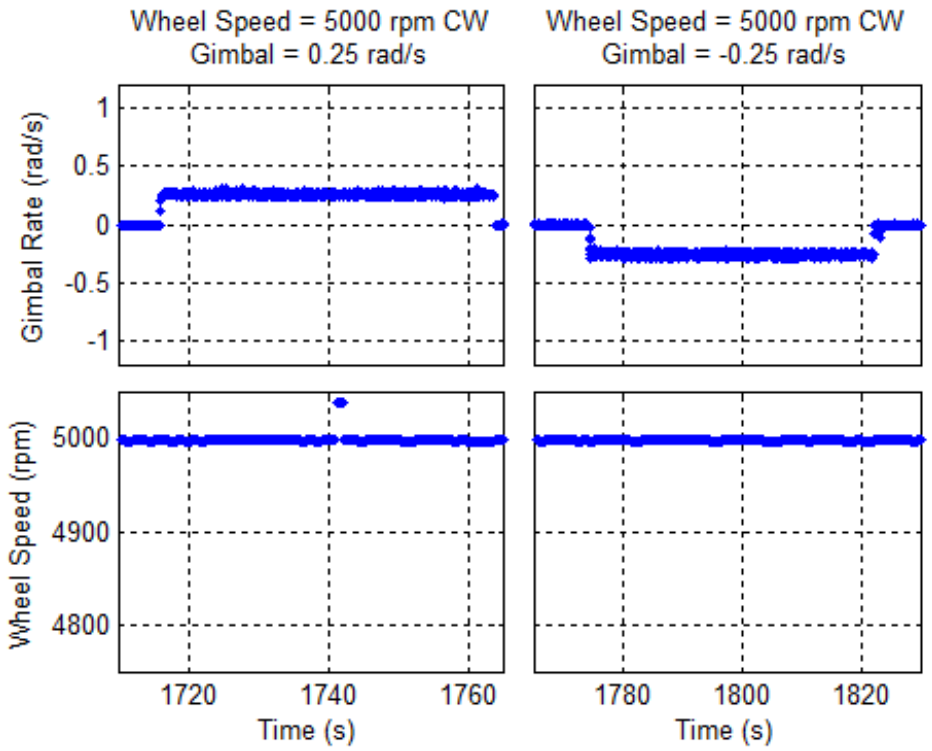

Figure 59. Momentum wheel speed with 0.25 rad/s gimbal rate, wheel spinning CW

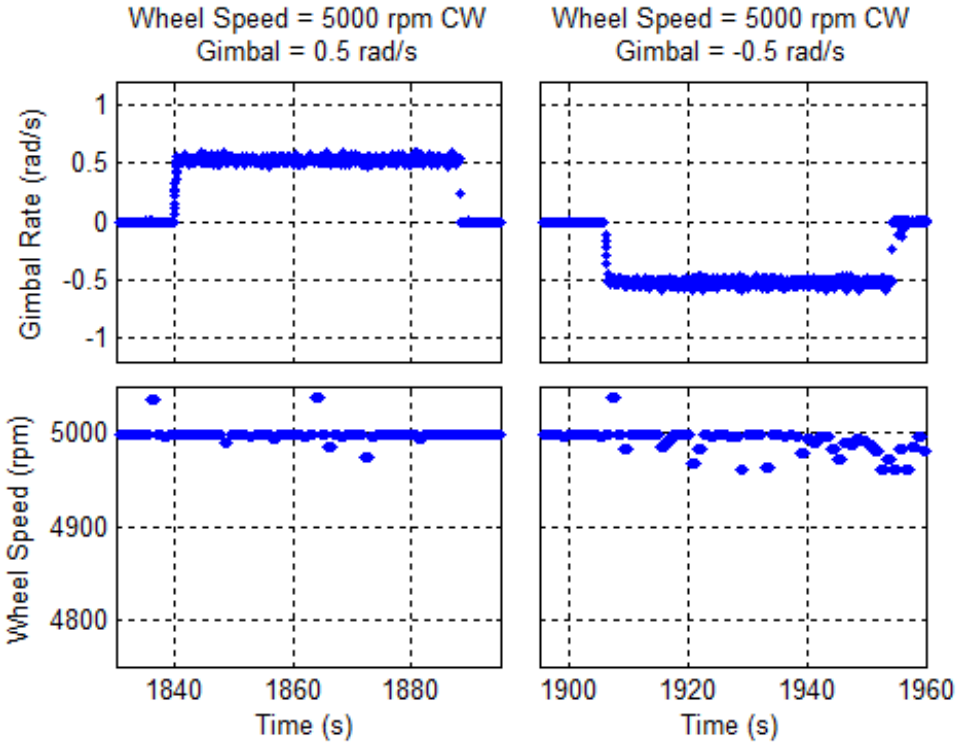

Figure 60. Momentum wheel speed with 0.5 rad/s gimbal rate, wheel spinning CW

In the 0.75 rad/s and 1.0 rad/s tests the magnitude of the speed dip is larger and begins soon after the gimbal rate reaches steady state. Even in the worst case with a 1 rad/s gimbal rate and the wheel spinning at 5000 rpm in the CCW direction, the dip is less than 200 rpm which only reduces the stored momentum by about 2%. Thus, the CMG is capable of holding the wheel momentum very close to nominal even during aggressive gimballing.

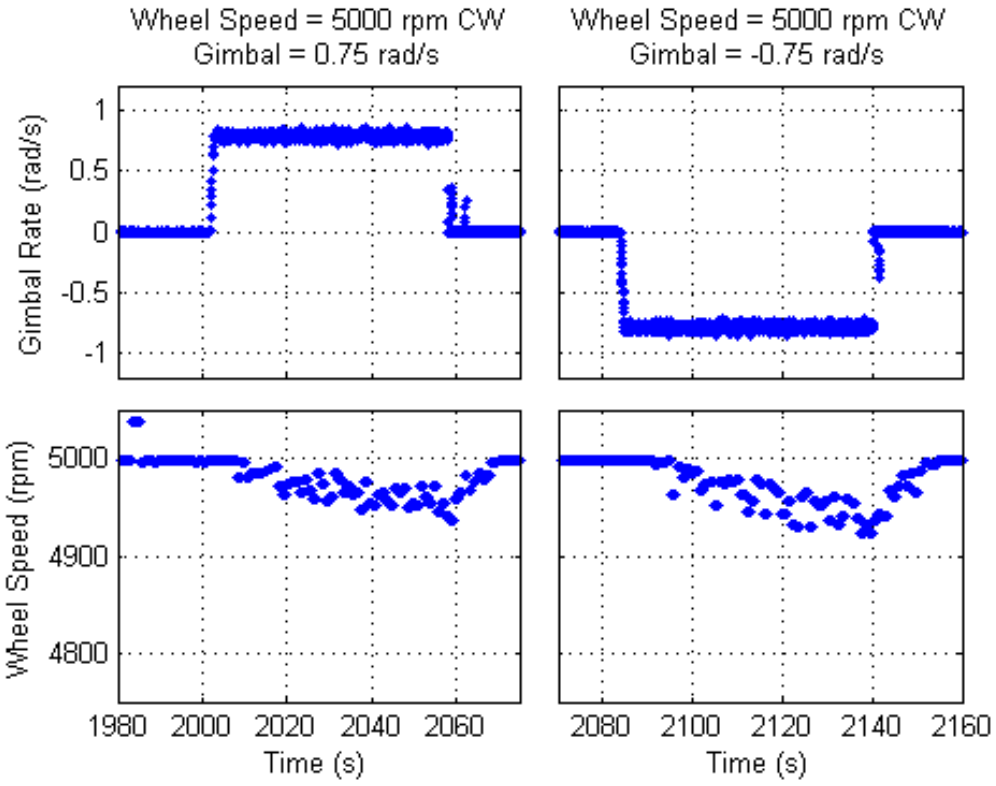

Figure 61. Momentum wheel speed with 0.75 rad/s gimbal rate, wheel spinning CW

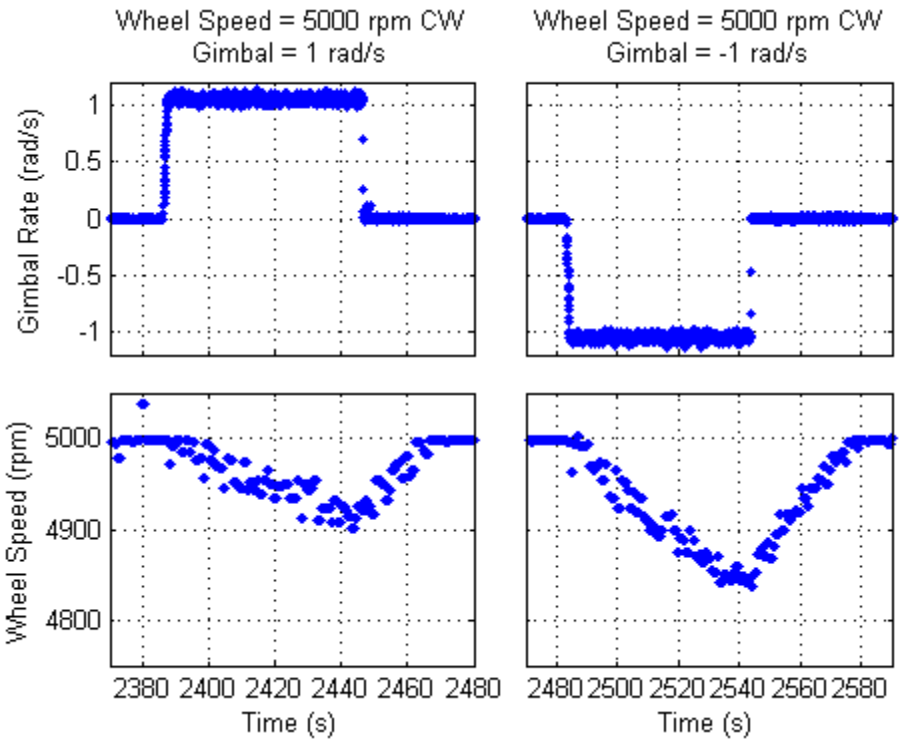

Figure 62. Momentum wheel speed with 1 rad/s gimbal rate, wheel spinning CW

G. SUMMARY

A series of characterization tests were run on the newly developed open architecture CMG to ascertain its performance. The gimbal motor was shown to be capable of providing gimbal rates of at least 1 rad/s, which meets the current industry standard. The momentum wheel motor was shown to be capable of reliably maintaining its desired speed of 5000 rpm within +0.1% and -2.0% even during aggressive gimballing.

Additionally, the CMG back drive phenomenon which is seldom discussed in textbooks was demonstrated. The maximum satellite rotation rates over which this CMG can maintain consistent control over the gimbal were calculated. To improve operation of the gimbal, the momentum wheel case should be balanced to eliminate the gravity torque effects. This CMG back drive also highlighted the importance of properly sizing the CMG gimbal drives to avoid the backdrive from becoming an overwhelming effect.

VI. CONCLUSION

A. SUMMARY OF WORK

The objective of this thesis was to design and characterize a prototype, open-architecture CMG that is a key part of a next generation ADCS testbed which will be installed on the NPS R-SAT. The primary design objectives were to develop a gimbal frame which can mount on the R-SAT, house the Ackman momentum wheel, and provide a continuous, manually adjustable skew angle. The iterative design process used for the gimbal frame consisted of CAD modeling of the hardware using NX 8.5, and rapid prototyping of the design in polycarbonate using a 3D printer. Once the design was fit checked and underwent initial functional checks, the finalized design drawings were provided to the machine shop for manufacture from 6061 aluminum plates.

The Ackman momentum wheel was integrated into the CMG frame with the Maxon EC45 gimbal motor, harmonic drive, and roller ball bearing. In addition to these components a pair of Maxon EPOS2 24/5 motor controllers were housed within the mount base structure with one mounted to the base plate of the mount base, and the second mounted to the horizontal plate of the gimbal frame to reduce the footprint of the integrated CMG system. In addition to the CMG design, a 3-DOF air bearing was modified with a custom collar which constrained two of the three rotation axes to create a 1-DOF air bearing for testing the CMG.

The CMG was run through a battery of characterization tests to assess its capabilities. The gimbal motor was shown to provide sufficient torque to gimbal the momentum wheel at rates up to at least 1 rad/s. The integrated encoder in the gimbal motor, when combined with the zero backlash 100:1 gear ratio harmonic drive, provided reliable and accurate gimbal position measurement. The initial assessment is that the 1024 counts/motor revolution (4096 quadrature counts/motor revolution) when combined with the harmonic drive gear reduction can provide gimbal position resolution of 3.2 arc-sec. This exceeds the performance of the optical encoder which was chosen for gimbal shaft position feedback.

The momentum wheel motor was demonstrated to be capable of holding the momentum wheel speed within +0.5/-2.0% of the 5000 rpm nominal operating speed even during extended 1 rad/s gimbal operations. The mass balance of the momentum wheel about the gimbal axis was shown to be biased toward the bearing side of the case. This imbalance will need to be corrected prior to ADCS integration due to the fact that the most common gimbal control input from the ADCS is motor current, without any gravity correction bias.

In addition to the design work, and characterization tests for the CMG an effort was made to understand and attempt to quantify the effects of a back drive torque created by the testbed rotation rate. Platform rotation rates as high as 7.2 °/s were calculated to be the nominal operational limit for this CMG, with a balanced momentum wheel housing. Peak rates of 79 °/s can also be accommodated for brief periods.

B. FUTURE WORK

In order to take this open architecture CMG design into phase 3 of the next generation ADCS development a number of tasks will need to be performed. The first of these tasks will be to balance the momentum wheel mass across the gimbal axis in order to allow the future ADCS the ability to accurately control the gimbal motor through motor current control inputs. Additionally, a more in-depth analysis of the accuracy of the Maxon integrated motor encoder for use in gimbal shaft position measurement will be necessary to determine whether an optical encoder mounted directly to the gimbal shaft will be necessary or not.

Finally, the CMG output torque should be characterized. This was one planned system characterization which was not completed successfully. Although the Razor 9-DOF IMU provided data which supported real-time test monitoring, the drift in the output data as well as the challenges of trying to calibrate it and properly filter the data using the BBB made the accuracy of the telemetry inadequate for CMG output torque measurement.

The next steps in building the evolved R-SAT will be to manufacture three more CMGs for installation on the R-SAT, and to mount them on the testbed. The motor controllers are expected to be connected via a CAN bus architecture, and the motor controllers will need to be connected and configured for use in this way. Although the BBB performed well for this single CMG testing, an appropriate R-SAT flight computer will need to be chosen and the Maxon motor controller source code will need to be configured for use on that system. The software for controlling all eight motors and motor controllers will need to be developed and implemented.

In addition to the code necessary to control the gimbal and momentum wheel motors, the CMG steering law will need to be designed and the next generation ADCS will need to be developed to implement that control law while simultaneously integrating the feedback inputs from the attitude determination sensors.

THIS PAGE INTENTIONALLY LEFT BLANK

LIST OF REFERENCES

[1] N. Bedrossian, S. Bhatt, W. Kang and I. M. Ross, "Zero-Propellant Maneuver Guidance," *Control Systems, IEEE,* vol. 29, no. 5, pp. 53–73, 2009.

[2] M. Karpenko, S. Bhatt, N. Bedrossian, A. Fleming and R. I. M, "First Flight Results on Time-Optimal Spacecraft Slews," *Journal of Guidance, Control, and Dynamics,* vol. 35, no. 2, pp. 367–376, 2012.

[3] K. Ackman, "Prototyping of an open-architecture CMG system," M.S. thesis, Naval Postgraduate School, Monterey, 2012.

[4] C. D. McManus, "Development, verification and experimental analysis of high-fidelity mathematical models for control moment gyros," M.S. thesis, Naval Postgraduate School, Monterey, 2011.

[5] Andrews Space, *3-DOF Satellite Simulator User's Guide,* Tukwila, WA, 2009.

[6] B. Wie, Space Vehicle Dynamics and Control, Reston: American Institute of Aeronautics and Astronautics, Inc, 1998.

[7] V. Lappas, W. Steyn and C. Underwood, "Experimental Testing of a CMG Cluster for Agile Microsatellites," *Journal-British Interplanetary Society,* vol. 57, no. 9/10, pp. 318–324, 2004.

[8] Maxon Motor, "EC 45 flat 42.8 mm, brushless, 50 Watt, with Hall sensors," Maxon Motor, [Online]. Available: http://www.maxonmotorusa.com/maxon/view/product/motor/ecmotor/ecflat/ecflat45/251601. [Accessed 3 March 2014].

[9] Harmonic Drive LLC, "Precision actuators, gearheads, and gearing components," 2012.

[10] Boston Gear, "Gear Theory," [Online]. Available: http://www.bostongear.com/pdf/gear_theory.pdf. [Accessed 29 November 2014].

[11] "Anker 2nd Gen Astro3 12000mAh External Battery Charger with PowerIQ," Anker, 4 November 2014. [Online]. Available: http://www.ianker.com/product/79AN7904S-BA. [Accessed 4 November 2014].

[12] Maxon Motor Ag, *EPOS2 24/5 Positioning Controller Getting Started,* December 2013 ed., Sachseln, Switzerland, 2013.

[13] M. Leszczynski, “Improving the Performance of MEMS Gyros via Redundant Measurements: Theory and Experiments,” M.S. thesis, Naval Postgraduate School, Monterey, 2014.

[14] SparkFun Electronics, “9 Degrees of Freedom - Razor IMU - SEN-10736,” [Online]. Available: https://www.sparkfun.com/products/10736. [Accessed 2014 December 2014].

[15] InvenSense, “ITG-3200 Product Specification Revision 1.4,” 30 March 2010. [Online]. Available: https://www.sparkfun.com/datasheets/Sensors/Gyro/PS-ITG-3200–00–01.4.pdf. [Accessed 13 October 2014].

[16] Analog Devices, “ADXL345(Rev. 0) - ADXL345.pdf,” May 2009. [Online]. Available: https://www.sparkfun.com/datasheets/Sensors/Accelerometer/ADXL345.pdf. [Accessed 13 October 2014].

[17] Honeywell, “HMC5883L-FDS.pdf,” March 2011. [Online]. Available: http://dlnmh9ip6v2uc.cloudfront.net/datasheets/Sensors/Magneto/HMC5883L-FDS.pdf. [Accessed 13 October 2014].

[18] MOOG, “SR73683,” MOOG, [Online]. Available: http://www.moog.com/products/slip-rings/commercial-industrial-slip-rings/slip-rings-with-through-bores/sra-73683/. [Accessed 4 November 2014].

[19] BeagleBoard.org, “BeagleBoard.org - latest-images,” 26 June 2014. [Online]. Available: http://beagleboard.org/latest-images. [Accessed 3 August 2014].

[20] EDIMAX, “Edimax EW-7811UN - 150 Mbps Wireless IEEE802.11b/g/n nano USB Adapter,” EDIMAX, [Online]. Available: http://www.edimax.com/au/produce_detail.php?pd_id=347&pl1_id=1&pl2_id=44. [Accessed 4 November 2014].

[21] Harmonic Drive LLC, “CSG High Torque Geahead,” [Online]. Available: http://harmonicdrive.net/products/gearheads/csg-unit/. [Accessed 26 November 2014].

INITIAL DISTRIBUTION LIST

1. Defense Technical Information Center
   Ft. Belvoir, Virginia

2. Dudley Knox Library
   Naval Postgraduate School
   Monterey, California